University of Alberta

DESIGN OF A FULLY-PRINTED BI-PLANAR VOLUMETRIC NEGATIVE-REFRACTIVE-INDEX TRANSMISSION-LINE METAMATERIAL

by

Hoang-Linh Nguyen

A thesis submitted to the Faculty of Graduate Studies and Research
in partial fulfillment of the requirements for the degree of

Master of Science

in

Photonics and Plasmas

Department of Electrical and Computer Engineering

Spring 2014
Edmonton, Alberta

Abstract

Since the first experimental demonstration of the negative-refractive-index metamaterial by Shelby et al. in the early 2000s, metamaterials have experienced great interest from research community, resulting in an increasingly large number of publications. Truly three-dimensional (3D) metamaterials, which are able to interact with electromagnetic sources from free space, have been targeted in much of metamaterial research. The physical implementation of such structures is often exorbitantly complicated. In some applications, which require free-space sources to be particularly polarized, 3D metamaterials can be replaced by volumetric metamaterials, which are an extension of 2D metamaterials in the third dimension, and are realized by stacking layers of 2D metamaterials. Volumetric metamaterials employ both surface-mount and fully-printed elements as reactive loads. Fully printed volumetric metamaterials are the most cost-effective because their fabrication is suitable for standard lithography processes. However, previous fully-printed structures suffered from weak reactive loads, resulting in a high operation frequency, hence, a large electrical length per unit cell. This thesis presents a bi-planar design utilizing MIM-type capacitors and dual-arm spiral inductors, which can easily be fabricated with normal printed-circuit-board technology, making it low-cost. The proposed structure operates at 4.4 GHz, resulting in a small electrical length of $\lambda_0/11$. The simulated data show that the structure can be treated as an isotropic effective medium possessing effective permittivity, permeability, and refractive index close to negative unity. The metamaterial may find applications as flat lenses in microwave hyperthermia, and in the improvement of antenna performance.

Acknowledgements

I would like to express my sincere gratitude to my supervisor, Prof. Ashwin K. Iyer, for his dedicated guidance and support for over the years. In three years, he has shown me his invaluable technical knowledge, his enthusiasm in research, his personality. I feel so grateful that I have him as my role model. I would also thank my colleagues Stuart Barth, Mianzhen Mo, Justin Pollock, Travis Schoepp, Yang Yu for their support during my experiments and the preparation for my thesis. Thanks also to two summer students, Hailey Pineau and Ian Thomson, who helped me set up my experiment.

Last but most importantly, I am indebted to my father, who passed away six months ago, mother and brother for their unconditionally love, support, and encouragement.

Hoang-Linh Nguyen

Edmonton, 2013.

Contents

List of Tables

List of Figures

List of Acronyms

2D :	Two-dimensional
3D :	Three-dimensional
BW :	Bandwidth
CPS :	Coplanar Stripline
DNG :	Double-negative
DPS :	Double-positive
EM :	Electromagnetic
ENG :	Epsilon-negative
IFFT :	Inverse Fast Fourier Transform
LH :	Left-handed
MIM :	Metal-insulator-metal
MNG :	Mu-negative
MUT :	Material Under Test
NRI :	Negative Refractive Index
PNA :	Performance Network Analyzer
PPW :	Parallel plate waveguide
PRI :	Positive refractive rndex
SCR :	Split-cube resonator
SGH :	Standard gain horn
SRR :	Split-ring resonator
TE :	Transverse electric
TL :	Transmission line
TM :	Transverse magnetic
TRL :	Through Reflect Line
TRM :	Through Reflect Match

Chapter 1

Introduction

Recent breakthroughs in technology have renewed the demand for novel materials, including those that may be unavailable in nature. For electromagnetic (EM) and microwave applications, this need involves materials that possess exotic electromagnetic properties, described by their permittivity (ϵ) and permeability (μ). These parameters measure the response of a medium to impinging EM waves due to its constituent atoms, or molecules. The permittivity represents how a medium responses to the establishment of the electric fields inside it, and the permeability describes the reaction of a medium to magnetic fields. Based on the sign combination of the permittivity and permeability, a material can be categorized as double-positive (DPS), epsilon-negative (ENG), mu-negative (MNG), and double-negative (DNG) media, corresponding to the four quadrants depicted in Figure 1.1 [1]. The propagation of EM waves inside a lossless medium is governed by a wavenumber, which is defined as $\beta = k = \omega\sqrt{\epsilon\mu}$. DPS media possess simultaneously positive permittivity and permeability ($\epsilon > 0$, $\mu > 0$), resulting in a real phase constant, hence, they support the propagation of EM waves. Most of the materials in nature belong to this category including dielectrics. Epsilon-negative (ENG) media have negative permittivity

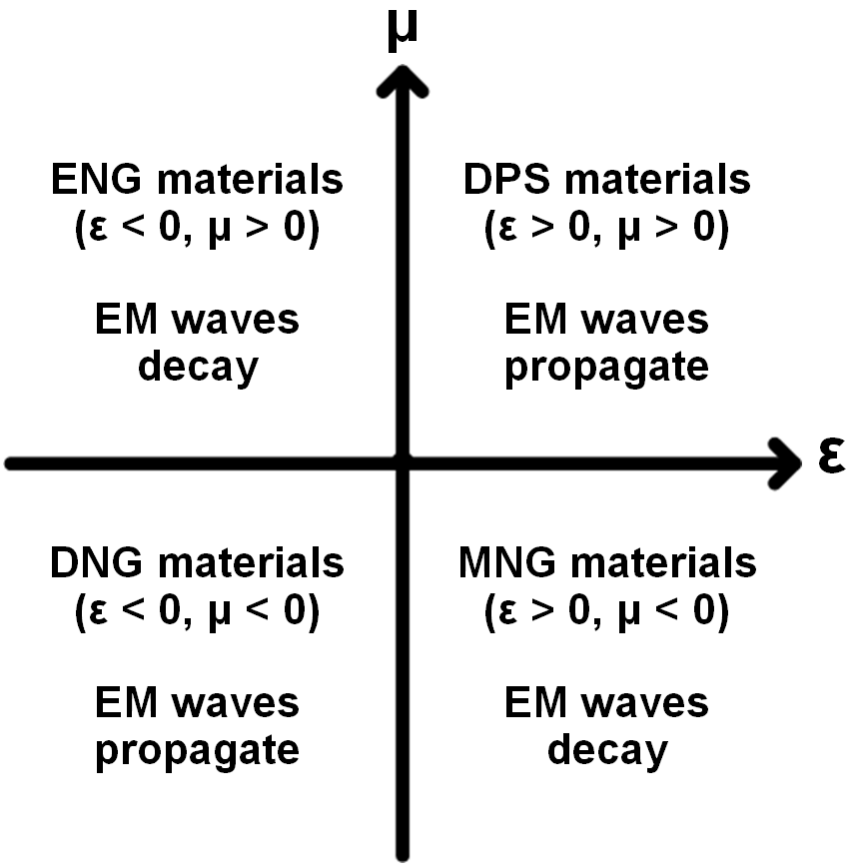

Figure 1.1: A classification of materials based on their permittivity and permeability.

($\epsilon < 0$) and positive permeability ($\mu > 0$), leading to an imaginary wavenumber, thus, preventing EM waves from traveling and instead causing them to decay. Such characteristics can be found in plasmas at particular frequencies, and in some synthesized media [2, 3]. A medium with positive permittivity ($\epsilon > 0$) and negative permeability ($\mu < 0$) is called a mu-negative (MNG) medium. This type of medium also yields a decay of electromagnetic waves, due to the imaginary phase constant. In a certain frequency range, some gyrotropic materials and artificial structures [4] possess this characteristic. The last category is the double-negative (DNG) medium, which has simultaneously negative permittivity and permeability ($\epsilon < 0, \mu < 0$). Theoretically, DNG media allow electromagnetic waves to propagate, and were first experimentally demonstrated with the composite DNG material in Ref. [5] just more than a decade ago, because such media are not available in nature.

1.1 DNG Media

A complete picture of DNG media was first hypothetically presented by Victor Veselago in the 1960s [6], who speculated that in such media ($\epsilon < 0, \mu < 0$) Maxwell's equations still hold provided that the electric field $\vec{E}$, magnetic field $\vec{H}$, and the wavevector $\vec{k}$ form a left-handed triplet [6]. Therefore, the wavevector $\vec{k}$ and the Poynting vector $\vec{S}$ are anti-parallel, as in Fig.1.2, because of the right-handed relationship between $\vec{E}$, $\vec{H}$, and $\vec{S}$ ($\vec{S} = \vec{E} \times \vec{H}$). The refractive index of a medium should generally be expressed in terms of its permittivity and permeability as $n = \pm\sqrt{\epsilon\mu}$, and the sign of the index should be chosen as " $+$ " if both ϵ and μ are positive, and " $-$ " if both ϵ and μ are negative [7]. The rationale behind this selection is apparent as we consider the permittivity and permeability of lossy media, which are expressed as $\epsilon = \epsilon' - j\epsilon''$ and $\mu = \mu' - j\mu''$, where the imaginary parts, ϵ'' and μ'', are conven-

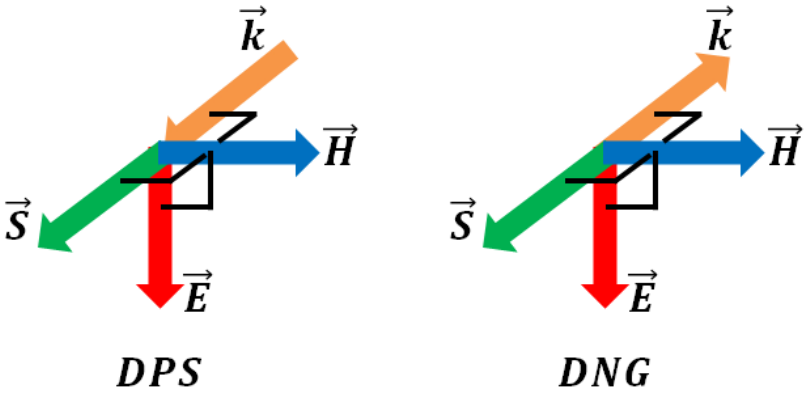

Figure 1.2: Orientation of Poynting vector, wave vector, electric field and magnetic field in both DPS and DNG media.

tionally positive for passive media. Similarly, the refractive index of the medium is also represented as $n = n' - jn''$, and satisfies the relationship $n^2 = \mu\epsilon$. Equating the imaginary parts of both sides yields $2n'n'' = \epsilon'\mu'' + \mu'\epsilon''$. If the real parts of the permittivity and permeability are negative (ϵ' and $\mu' < 0$), and the medium is passive (ϵ'', μ'', and $n'' > 0$), it is clear that the refractive index of the medium n' must be negative, and $n = -\sqrt{\mu\epsilon}$.

1.1.1 Negative Refraction

The simultaneously negative parameters of DNG materials produce the phenomenon of negative refraction, which is observed when a EM wave propagates through the interface between a DNG medium and a DPS medium. As shown in Figure 1.3, the incident wave from a DPS medium arrives at the border with a second medium. At the boundary, the phase matching condition requires that the tangential components of both incident and refracted waves are equal ($\vec{k_{ti}} = \vec{k_{tr}}$). Hence, there are two possibilities for the normal components: case 1 - forward ($\vec{k_{nr1}}$), which corresponds

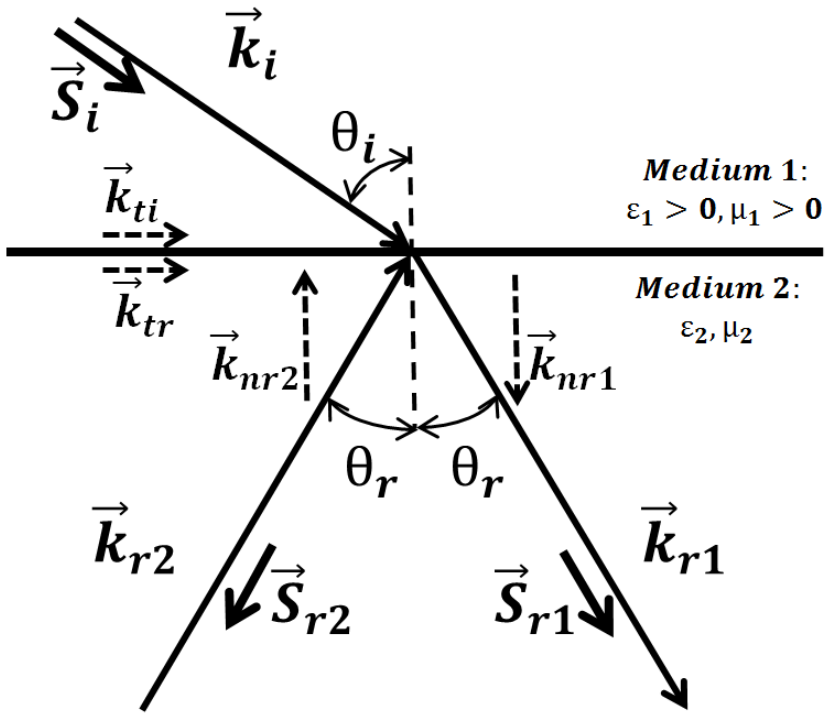

Figure 1.3: Refraction at the interface between two media: case 1 for positive refractive index media denoted by subscript 1, and case 2 for negative-refractive-index media by subscript 2.

to positive refraction ($\vec{k_{r1}}$), and case 2 - backward ($\vec{k_{nr1}}$), which represents negative refraction ($\vec{k_{r2}}$). The refraction angles have the same absolute value $|\theta_r|$ for both cases. It should be noted that in DNG media, the requirement that the wave energy advances from the first medium to the second medium results in the wavevector $\vec{k_{r2}}$ and the Poynting vector $\vec{S_{r2}}$ being anti-parallel.

1.1.2 Flat-lens Focusing

Applying the negative-refraction phenomenon at the interface between DPS and DNG media, an intriguing device, a flat lens without an optical axis, was proposed by

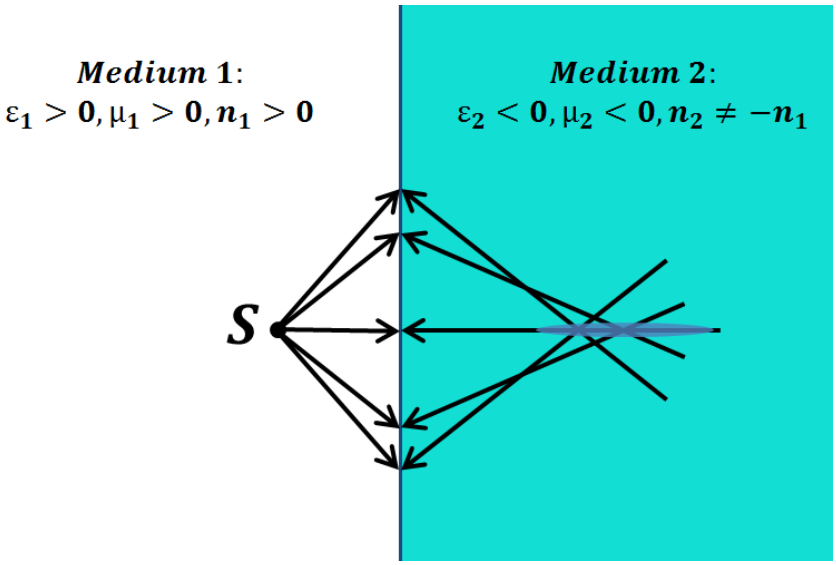

Figure 1.4: A point source creates a plane image in a DNG medium due to $n_2 \neq -n_1$.

Veselago [6]. The refraction of a point source in a DPS medium through a slab of DNG medium was investigated. The refraction relationship at the interface of a DPS medium and a DNG medium is defined as

$$\frac{sin\theta_i}{sin\theta_r} = -\sqrt{\frac{\mu_2\epsilon_2}{\mu_1\epsilon_1}}, \tag{1.1}$$

If the refractive indices of the DNG and DPS media do not have the same absolute value, the point source in the DPS medium creates aberrations in the focal spot inside the DNG medium (Figure 1.4). Therefore, Veselago deliberately chose the refractive index of the media as $n_{DNG} = -n_{DPS} = -1$, so that the DNG slab is able to interact with source from free space, which is the DPS medium. As shown in Figure 1.5, the point source creates an image through the slab because of negative refraction without any geometric aberration, thus, rendering the slab a flat lens. Furthermore, the distance from the source to the image was twice as much as the slab thickness (or $s_1 + f_2 = d$). Pendry, moreover, added in his publication [8] that such a lens

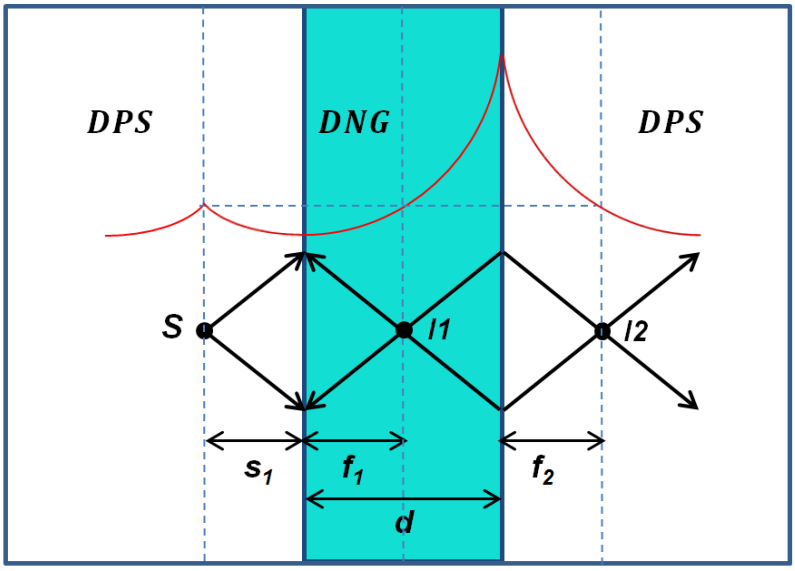

Figure 1.5: Focusing of a cylindrical source from one DPS medium to another DPS medium through a slab of DNG material.

has the ability to restore the amplitude of evanescent waves, which contain the finest features of the source, but typically decay strongly in the near-field range, resulting in an imaging ability that overcomes the diffraction limit. The red curves in Figure 1.5 depict that the magnitude of evanescent waves of the source; the restoration of the evanescent amplitudes at the first and second images ($I1$ and $I2$) is evident.

Veselago also discussed other phenomena in these media such as a negative Cerenkov radiation, and a negative Doppler effect. Besides simultaneously negative permittivity and permeability, DNG media have the left-handed relationship between $\vec{E}$, $\vec{H}$, and $\vec{k}$, the anti-parallel relationship of $\vec{k}$ and $\vec{S}$, therefore, they are also termed left-handed (LH), backward-wave, or negative-refractive-index materials, and widely recognized in the electrical engineering and physics communities as "*metamaterials*". It is also worth mentioning some prior work that contributed to the vision of DNG media by Lamb et al.[9], Schuster et al. [10], Mandel'shtam et al. [11], Pafomov et al. [12].

Veselago acknowledged that plasmas could provide negative permittivity; however, he did not point out any material, which could be both isotropic and provide negative permeability. The answer for his unsolved question was actually found in the artificial-dielectric approach. It is worth looking back at the history of the artificial dielectrics prior to metamaterials.

1.2 Artificial Dielectrics

The earliest work on artificial dielectrics could be dated back to the end of nineteenth century when Bose attempted to rotate the polarization of electromagnetic waves with his man-made chiral material of twisted fibers mimicking the natural chirality of sugar [13]. Similarly, Lindman, in 1920, synthesized chiral media by coiling small helices from copper wires [14]. However, the seminal work on artificial dielectrics was published by W. E. Kock from Bell Laboratories in the late 1940s. He introduced the metal-lens antenna, which used metal lenses consisting of metal plates, producing a phase velocity higher than speed of light, to shape the beam of antennas. As a result, the metal lens possessed a less-than-unity refractive index [15]. The waves propagating through the lens resembled TE modes in parallel-plate waveguides, for which the electric field is parallel to the waveguide's plates. Maintaining the advantage of light weight, Kock realized another metallic delay lens, which employed electrically small metallic disks periodically arranged in the shape of a convex lens [16] as a substitution for bulky and heavy natural-dielectric lenses. Unlike the previous metal lens, this design possessed the phase-delay property of natural dielectrics, i.e. its effective index of refraction was larger than unity. Inspired by the idea of imitating the behaviours of a molecular lattice of nature materials to light waves, he synthesized these materials from conducting strips, spheres, and disks operating in the microwave regime. He

established an analogy between the engineered lattice of metallo-dielectric scatterers and natural lattices, such that the free electrons in the conductors travel back and forth in the alternating electric field, producing oscillating dipoles similar to molecular dipoles of the natural dielectrics. Therefore, he coined the term "artificial dielectrics" for this new class of composite materials. There are two requirements for artificial dielectrics to be treated as effective media. Firstly, the spacing between the elements must be much smaller than the shortest wavelength in the operating band. This condition prevents the occurrence of diffraction, which is analogous to X-ray diffraction in crystalline solids. Secondly, the dimension of the elements themselves must be less than half of the minimum wavelength to avoid structural resonance effects. Ideally, the size should be as small as possible, so that the engineered materials are consistent over broad range of frequency. Once these conditions are satisfied, the response of the constituents of the media to the electric and magnetic fields of the propagating waves can be macroscopically considered in terms of effective permittivity and permeability. The effective-medium condition suggests that it is unnecessary to tailor materials at the molecular level, and the use of artificial dielectrics, whose periodicity is much smaller than the operating wavelength, suffices, particularly for microwave, millimeter-wave, and terahertz applications, where the individual scatterers may be more easily designed.

Cohn further contributed to artificial-dielectric research by modeling a metal-strip lens, which was experimentally demonstrated by Kock [16], using transmission-line low-pass filters [17]. Cohn also proposed a procedure for selecting physical parameters for strip medium to obtain perfect match to free space at a particular frequency, and extended the procedure for different shapes of metallic objects. Finally , he experimentally compared his model with others in the literature to affirm its validity over a wider range of frequencies [18]. After Kock and Cohn, the research on artificial

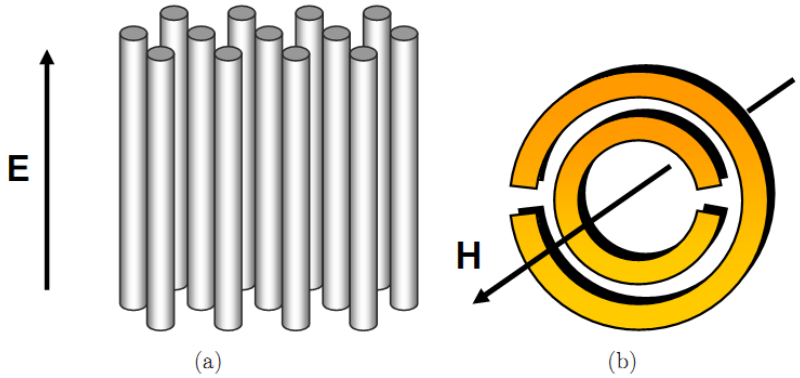

Figure 1.6: (a) An array of thin wires possessing plasma-like behavior with ($\epsilon < 0$); (b) A SRR with capacitive slots producing ($\mu < 0$) [7].

dielectrics was extended by Brown, Collin, etc. to classify artificial dielectrics based on their effective index of refraction, the shapes of their constitutive elements; and characterization of the artificial dielectrics with Lorentz theory and transmission-line theory to explain the behaviors of EM waves at the interface between these media and free space [19, 20]. Along with the development of a robust and powerful theory, artificial dielectrics also contributed greatly to several radar applications from the 1940s to the 1970s.

1.3 Metamaterials Using Resonant Elements

In 1962, Walter Rotman proposed his artificial dielectrics of inductive thin wires for application to modeling plasma-like media (Figure 1.6a). He pointed out that the lossy rodded media possess a plasma frequency (ω_p), below which the refractive index of the media is less than unity. Unlike Rotman, who never explored the negative-permittivity region, John Pendry independently discovered the structures, emphasizing that the "very thin wires dilute the average concentration of electrons and

considerably enhance the effective electron mass through self-inductance", hence, he employed them as negative-permittivity media [3]. Apart from the thin-wire medium, he suggested that the effective permeability of an array of concentric rings could be tuned with appropriate gaps producing capacitive loads, resulting in a resonant negative effective permeability [4]. These capacitively loaded loops were termed split-ring resonators (SRRs) (Figure 1.6b), and employed as negative-permeability media. Finally, three decades after the question about practical realization of metamaterials was first raised, Shelby, Smith, and Schultz proposed the solution as a combination of an array of thin wires and SRRs, as shown in Figure 1.7, and the first experimental demonstration was conducted in the early 2000s [5]. Shelby et al. implemented the negative permittivity and negative permeability media on a fiberglass substrate with square SRRs on one side and metal strips, representing the thin wires, on the other side. The fabricated boards were arranged in a prism shape. The experiment illustrated a negative effective refractive index of -2.7 ± 0.1 at 10.5 GHz as the result of simultaneously negative effective permittivity and permeability, and exhibited the reversal of Snell's law.

1.4 Metamaterials Using Negative-Refractive-Index Transmission Lines

An alternative approach for synthesizing metamaterials is based on transmission-line models using lumped-elements. The simplest model of LH media employs a high-pass configuration of inductors and capacitors, which is widely known to support backward-wave propagation [21]. This model can be obtained by interchanging the positions of the inductive and capacitive loads in the conventional TL model [22]. In

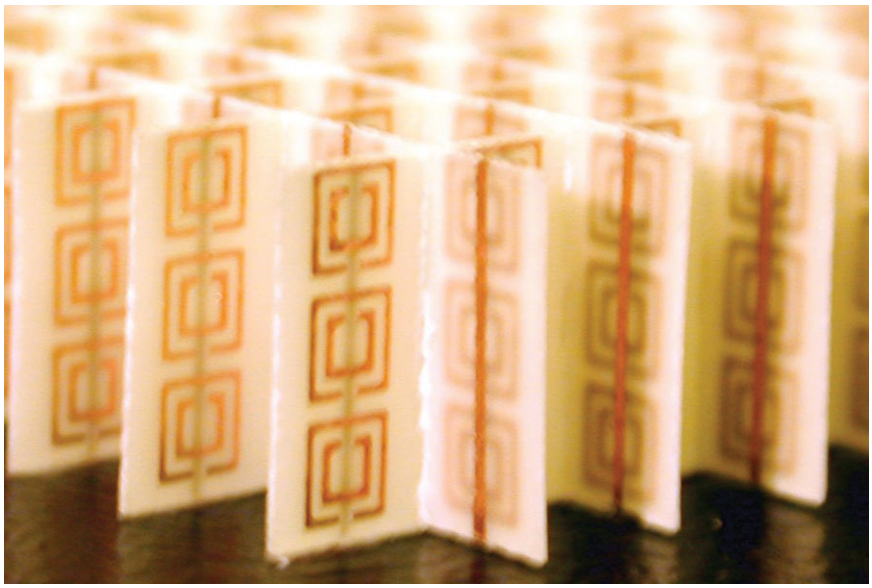

Figure 1.7: A depiction of the first wire/SRR metamaterial [5].

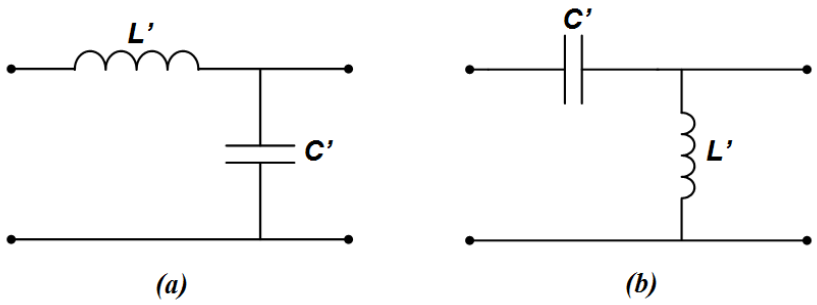

Figure 1.8: Transmission-line model of (a) RH medium, (b) LH medium.

these models (Figure 1.8) the effective permittivity and effective permeability corresponds to the shunt and series branches, respectively. In other words, the shunt capacitors and series inductors describe positive effective parameters, whereas the shunt inductors, and series capacitors correspond to negative effective parameters. Although the existence of the purely LH materials, which are modeled by the high-pass configuration, cannot be found in reality, the negative-refractive-index transmission-line (NRI-TL) materials can be constructed by loading periodically a host transmission

line with capacitors in series and inductors in shunt [23]. The loading capacitance C_0 and inductance L_0 are calculated, so that they overwhelm the intrinsic parameters, i.e. shunt capacitors and series inductors, of the host TL simultaneously over a certain range of frequencies, resulting in the simultaneously negative effective permittivity and permeability. The host TL, whose per-unit-length inductance and capacitance are L' and C', respectively, should have its periodicity d small enough to be considered an effective medium; hence, the loaded TL may be appropriately represented by the lumped model shown in Figure 1.9. At low frequencies, the intrinsic elements dominate, as the frequency increases, the loading elements gradually negate the intrinsic parameters of the TL host, resulting in an LH medium, which has series capacitors C_{LH} and shunt inductors L_{LH} over a specific frequency range. Because the shunt and series branches in the model, which describe a material's constitutive parameters, of the NRI-TL metamaterials are frequency dependent, making them dispersive.

1.4.1 Two-Dimensional Metamaterials

Two-dimensional NRI-TL metamaterials are an extension of the one-dimensional NRI TL, which has been studied in Refs. [21, 24], and can be implemented in two fashions: the shunt-node topology (Fig. 1.10a) and the series-node topology (Fig. 1.10b). The 2-D metamaterials based on shunt-node topology was implemented by loading shunt inductors and series capacitors to a perpendicular grid of microstrip lines. These 2D NRI-TL metamaterials were rigorously analyzed in Ref.[23] to obtained formulas for their effective parameters. In 2002, Eleftheriades et al. introduced the first experimental verification of the focusing ability of a 2D NRI-TL metamaterials [23]. A number of implementations of this topology and numerical verification of its negative-refractive-index properties were introduced in Refs.[23, 25, 26].

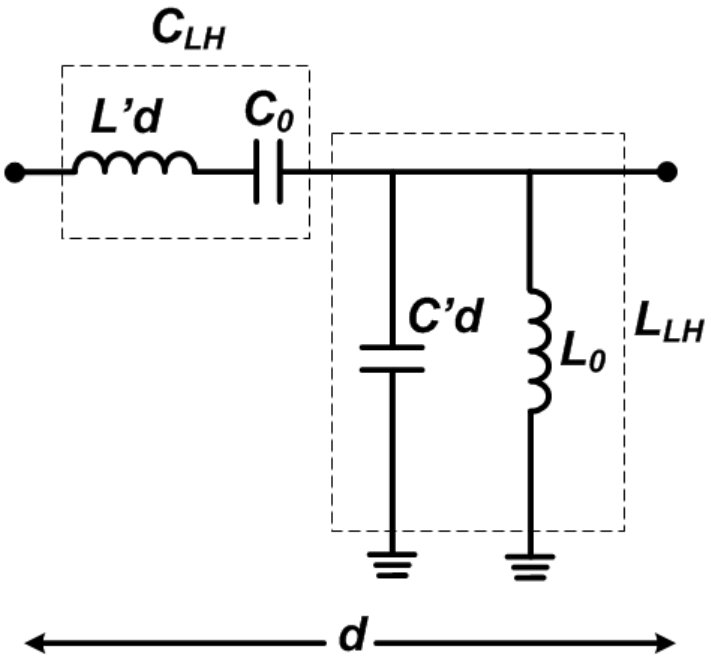

Figure 1.9: LH-medium model for practical NRI-TL metamaterial: capacitive load C_0 in series with TL-host inductance $L'd$ and inductive load L_0 in shunt with TL-host capacitance $C'd$ resulting in capacitive series branch (C_{LH}) and inductive shunt branch (L_{LH}) at particular frequencies.

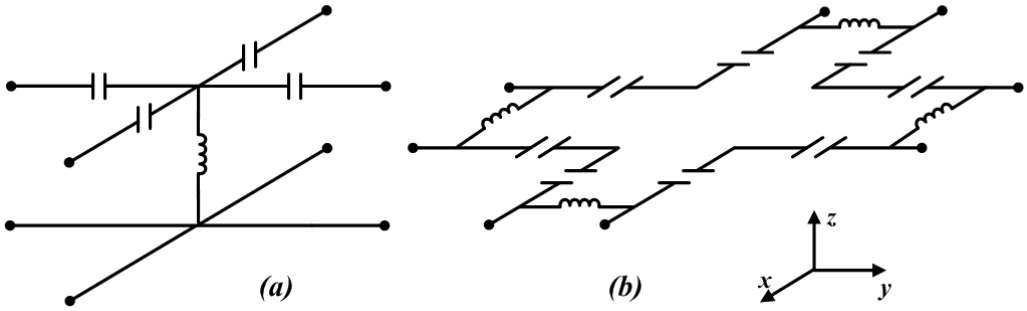

Figure 1.10: (a) the 2D shunt-node unit cell; (b) the 2D series-node unit cell.

The 2D series-node NRI-TL metamaterials were also studied in Refs.[27, 28] using the periodic analysis, which based on Bloch's theorem. One unit cell, which is depicted in Figure 1.11, consists of four segments in both x and y directions. Each segment of

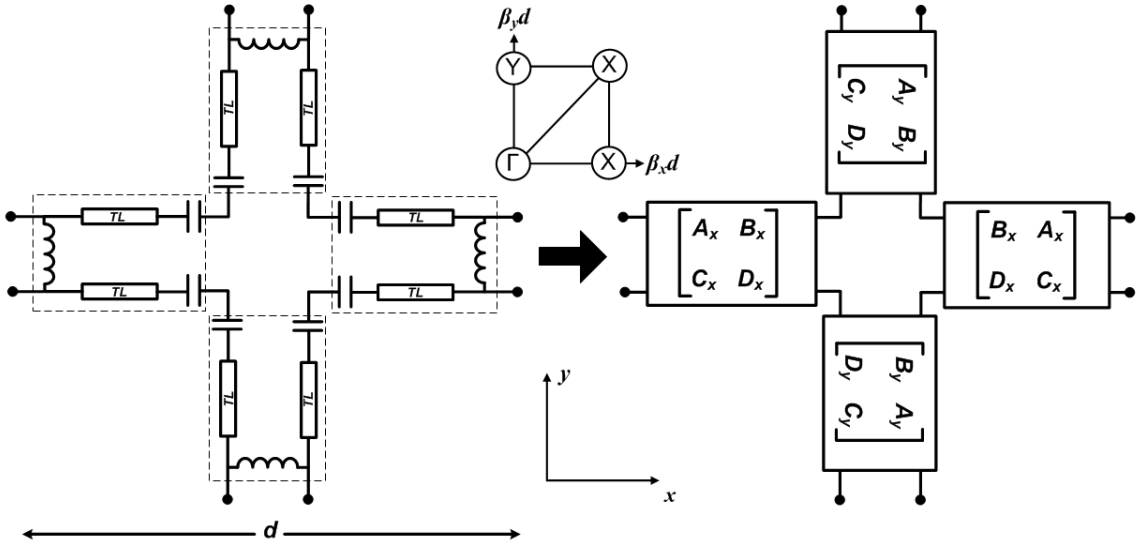

Figure 1.11: Representation of one unit cell as ABCD matrices.

the loaded TL is described as an ABCD matrix, whose entries depend on the values of the host TL and reactive loads. Hence, the dispersion relation can be expressed as

$$A_y C_y[(1-\cos\beta_x d)+2B_x C_x]+A_x C_x[(1-\cos\beta_y d)+2B_y C_y]=0, \tag{1.2}$$

where β_x and β_y are propagation constants along x and y directions, respectively. Based on the dispersion relationship (1.2) and the effective-medium assumptions, the 2D effective permeability (μ_{eff}), and permittivity (ϵ_{eff}) of the metamaterials can be obtained as follows [28]

$$\mu_{eff}=2\mu_p-\frac{1}{\omega^2 g C_0 d}, \tag{1.3}$$

$$\epsilon_{eff}=\epsilon_p-\frac{g}{\omega^2 L_0 d}. \tag{1.4}$$

where μ_p, and ϵ_p are the permeability and permittivity of the medium filling in the

TL host, which are proportional to the per-unit-length inductance and capacitance of the host; C_0, and L_0 are reactive loads, g is the geometric factor, and d is the loading periodicity. The series-node NRI-TL metamaterials are realized using coplanar striplines (CPS) as host TLs.

1.4.2 Volumetric NRI-TL Metamaterials

2D metamaterials have shown their imaging ability, where the NRI medium is interfaced with positive-refractive-index (PRI) media or conventional TL grid [23]. However, in these arrangements, the metamaterials only interact with sources embedded in the TL network rather than those in free space. Therefore, a need for 3D metamaterials has arisen. Several attempts have been made to construct 3D-isotropic metamaterials. In 2005, Grbic et al. proposed a topology for 3D metamaterial, in which the shunt-node NRI-TL based metamaterial was extended to third dimension, yielding good free-space matching in simulation [29]. In the same year, Yee's FDTD-cell based metamaterials [30] consisting of a transmission line scheme loaded with appropriate shunt and series reactive loads was simulated. The use of Kron's topology [22] was consistent through Alitalo's , Zedler et al.'s, or Iyer et al.'s structures. However, they are not isotropic [31], or are too complicated for fabrication [32, 33]. In 2012, Rudolph et al. experimentally demonstrated a broadband 3D isotropic NRI medium [34], which employed split-cube resonators (SCR) as a unit cell. The medium possessed a bandwidth more than twice that of SRRs, but the structure was not suitable for implementation using standard lithography processes.

Another direction for free-space metamaterials is that of volumetric NRI-TL metamaterials, which are an extension of 2D NRI-TL metamaterials. These type of metamaterials can be realized by stacking layers of 2D NRI-TL materials, so that a suitably

polarized source, normally a cylindrical line source, can be employed to excite such materials. Most of these metamaterials can be realized by standard PCB processes. Polarization of the metamaterials varies from TM waves [35, 36], i.e. where the magnetic field is perpendicular to the material plane, to TE waves [37, 38, 39, 40], i.e. where the electric field is perpendicular to the material plane, or both [41].

1.4.3 NRI-TL Metamaterial Applications

Metamaterials provide a great potential for many applications in both the microwave regime and optical regime; however, this section is limited to those of NRI-TL metamaterials. NRI-TL based metamaterials have found applications in lenses, microwave devices, and antennas.

NRI-TL metamaterials can be found in design of phase shifters, couplers, and dividers [7]. The NRI-TL metamaterial-based phase shifters consist of alternating sections of positive-refractive-index TL, i.e. normal TLs, and NRI TLs, so that, the phase shift of the device may be zero, due to the compensation of the positive phase of PRI-TL sections and negative phase of NRI-TL sections. Therefore, the total length of the phase-shifter is much smaller than one s wavelength of the operating frequency, which is required for a zero-degree phase shift in conventional phase shifters. The NRI-TL metamaterial-based couplers and dividers have also shown a significant size reduction. Besides, the NRI-TL metamaterial coupled-lined couplers also reveal an intriguing phenomenon of contradirectional power flow when lines are phase-matched.

The well-known designs of NRI-TL metamaterial-based antennas are leaky-wave antennas. These antennas are designed to have backward-wave and forward-wave properties in the fast-wave region, or radiation region. As the frequency varies, their beam direction changes from negative angles to positive angles, suggesting beam-

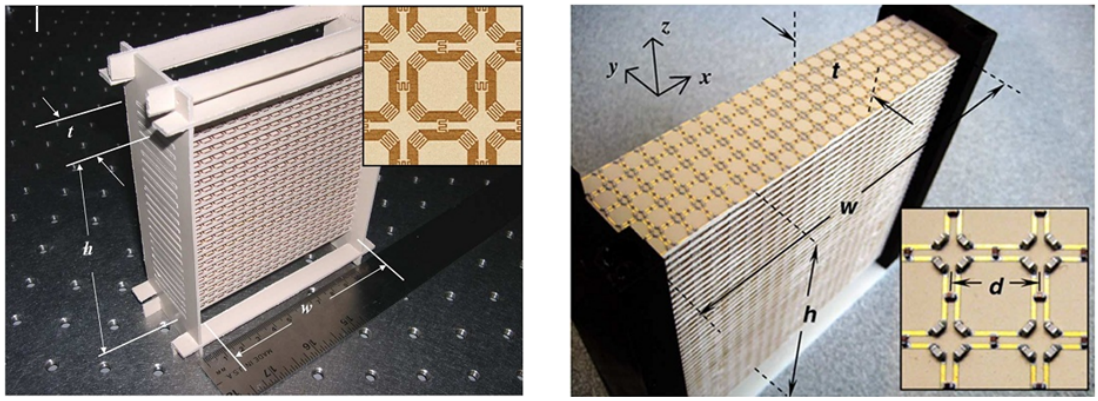

Figure 1.12: (a) The fully-printed volumetric NRI-TL with series interdigitated capacitors and meandered-line inductors; (b) The superlens based on volumetric NRI-TL metamaterials employed surface-mount capacitors and inductors [35, 36].

scanning ability. These tunable leaky-wave antennas can use both active and passive components for loading [7]. One design was reported to reduce beam squinting in a particular range of frequencies [42]. These antennas are printed-circuit-board (PCB) based, hence, they are easy to integrate with other PCBs, or be mounted on aircrafts or vehicles. Furthermore, NRI-TL metamaterials were employed to miniaturize antennas by miniaturizing their feed networks, resulting in a miniaturization of the total size of the designed antenna [43]. Besides these, several 'metamaterial-inspired' antennas were also reported to possess electrically small dimensions [44, 45]

1.5 Motivation

There are several proposed structures and methods that have been developed in the attempt to obtain volumetric metamaterials, which are able to interact with particular sources in free space. In 2007, a fully-printed volumetric NRI-TL metamaterial

structure was experimentally verified, possessing NRI properties at X band [35]. This structure utilized weak loading elements of interdigitated capacitors and meandered-line inductors (Figure 1.12(a)) resulting in a large electrical unit-cell size ($\lambda_0/5$), which challenged the effective-medium condition. In 2009, Iyer et al. solved the problem with the employment of high-quality surface-mount inductors and capacitors (Figure 1.12(b)) achieving a small electrical unit-cell size of $\lambda_0/18$, and producing a volumetric NRI-TL metamaterial superlens that overcame the diffraction limit [36]. However, the fabrication of the structure is prohibitive due to the cost of loading components and the assembly of those components to the PCBs. Other attempts on volumetric metamaterials have been made, some topologies require commercial chip components as reactive loads [34, 37, 41]. Other topologies are suitable for standard PCBs fabrication, however, they either operate at high frequency (X band) [40], or possess a parasitic parallel-plate mode that couples to the backward-wave mode, creating an unwanted bandstop condition [38]. The motivation of this project is to design an improved fully-printed volumetric NRI-TL metamaterial with stronger loading using metal-insulator-metal (MIM) type capacitors and double dual-arm spiral inductors, which can easily be fabricated using normal lithography processes, making it low-cost. The use of MIM-type capacitors confine the electric field between their two parallel plates, providing more capacitance than the fringing-field interdigitated capacitors. Moreover, the capacitance can be easily varied by modifying the dimensions of the plates. In order to accommodate the MIM-type capacitors, the proposed structure becomes bi-planar in nature, in which both sides of the substrate are metallized. In Chapter 2, a representative structure is introduced as a pilot design to identify its potential problems. After that, an extended theory and methodology for the design of bi-planar volumetric NRI-TL metamaterials, their dispersion relation, and parameter retrieval to obtain the effective permittivity and permeability, are presented.

Chapter 3 presents a design procedure and optimization approach to obtain the optimum structure that achieves a NRI band around 4.4 GHz, yielding a small electrical length of $\lambda_0/11$, and demonstrating high reactive loading values of the printed components (MIM-type capacitors and dual-arm spiral inductors). Chapter 4 describes the fabrication and measurement of the optimized design.

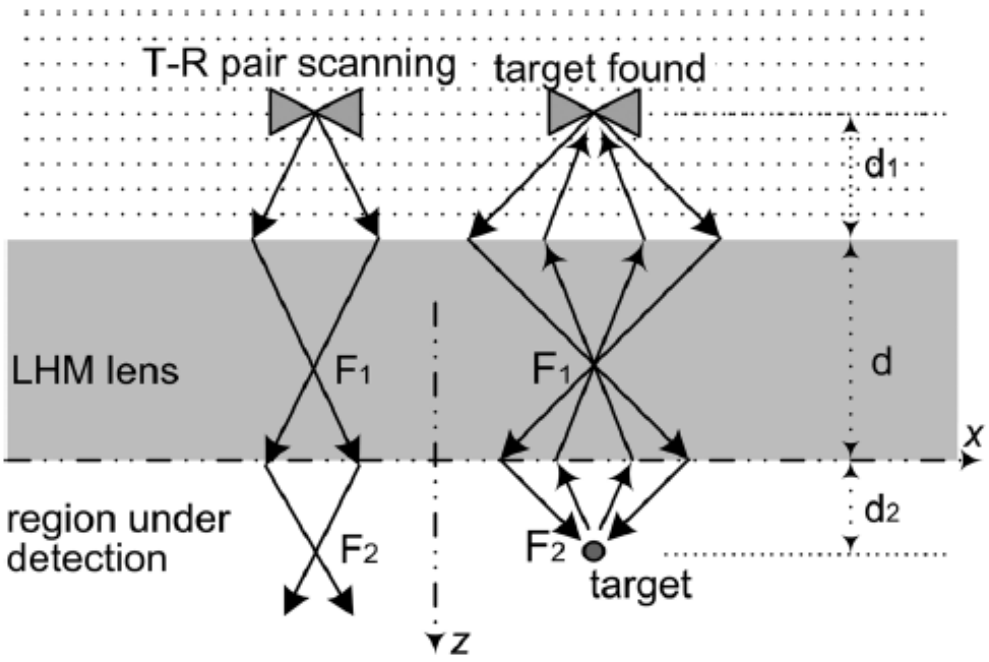

Figure 1.13: The scanning scheme to detect target tissues with a flat lens [46].

The proposed structure finds potential applications in microwave hyperthermia, and radiation-pattern improvement of antennas. First, the resolution beyond the diffraction limit was credited to flat, low-loss NRI-TL metamaterial superlenses [36, 39], which require very stringent design. Although the flat metamaterial lenses' performance is degraded by losses, they can still be employed for concentrating microwave energy, for example, in the hyperthermia of superficial cancerous tumors, in which moderate-size focusing points are targeted, rather than the hyperthermia for early-

stage small-size tissues [46]. The scanning scheme with a flat lens is depicted in Figure 1.13. It can be controlled by linearly moving the source in lateral and longitudinal directions, so that the image can find the target. This gives flat lenses advantages over conventional lenses, which demand complex and precise control mechanism because of their principal axes. Second, flat lenses focus the EM fields because of their negative refractive index, hence, they can be installed in the radiation direction of the antennas to guide the propagating waves. As a result, the radiation pattern of the antennas can be improved [47]. It should be noted that the flat lens is suitable for particular polarization of the EM waves, and the integration of the lens with antennas should take this into account.

Chapter 2

Representative Design and Theory

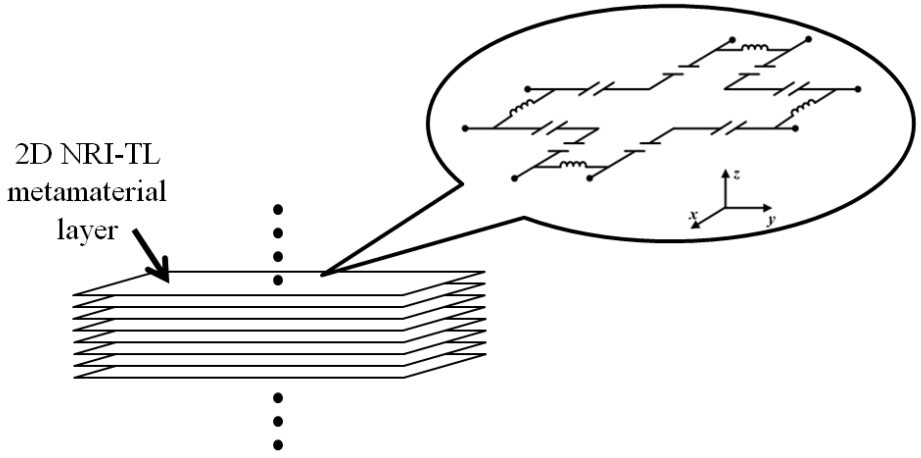

Figure 2.1: Stacking of 2D NRI-TL series-node based metamaterial layers creating a volumetric structure.

Volumetric metamaterials are realized by stacking 2D layers of NRI-TL metamaterials, as shown in Figure 2.1. Although this type of material cannot isotropically interact with an arbitrary source in free space, it may be designed to couple to particularly polarized 2D waves in free space such as cylindrical waves. The suitable polarization for the following design is the TE polarization, which has electric fields parallel to, and magnetic fields perpendicular to, the metamaterial-layer planes. A

different view of the series-node based metamaterial unit cell is obtained by a half unit-cell transition in the transverse directions, so that the unit cell is recognized as a ring loaded with capacitors at its four corners and connected to other rings by inductors, as shown enclosed by the dashed lines in Fig.2.2.

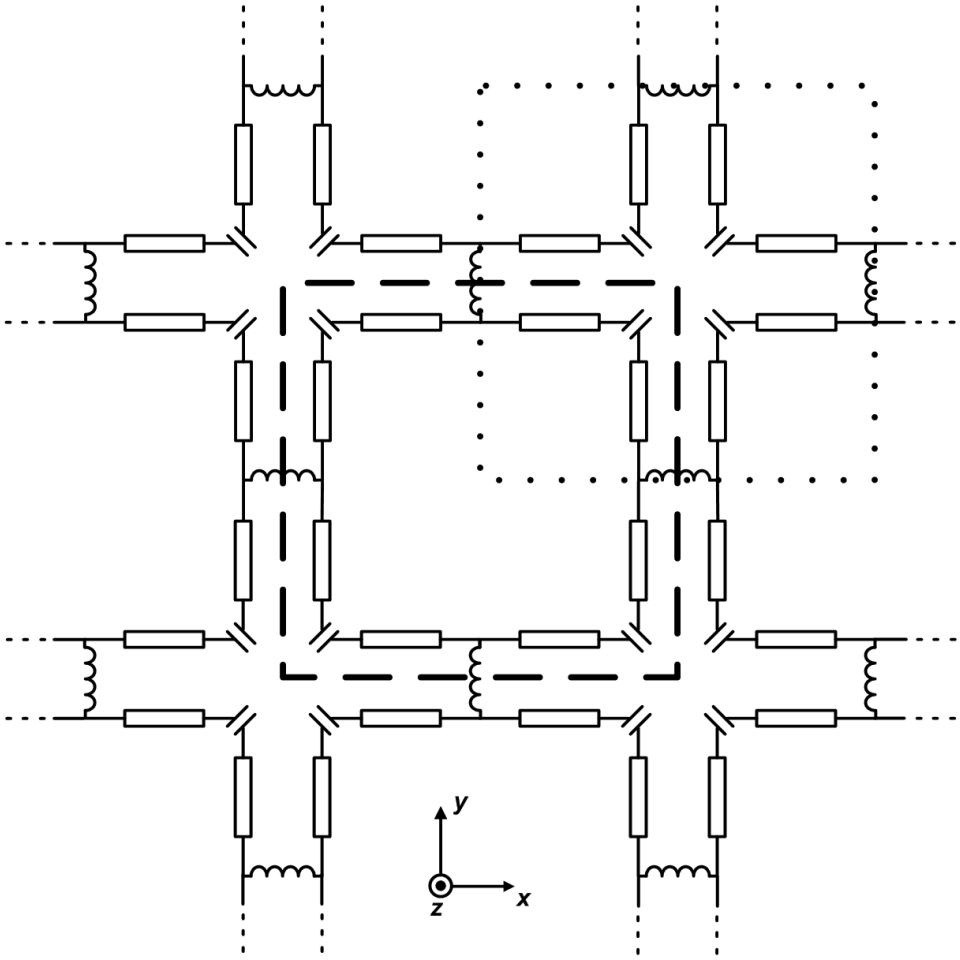

Figure 2.2: Two different perspectives of the series-node NRI-TL metamaterial unit cell indicated by dotted and dashed squares.

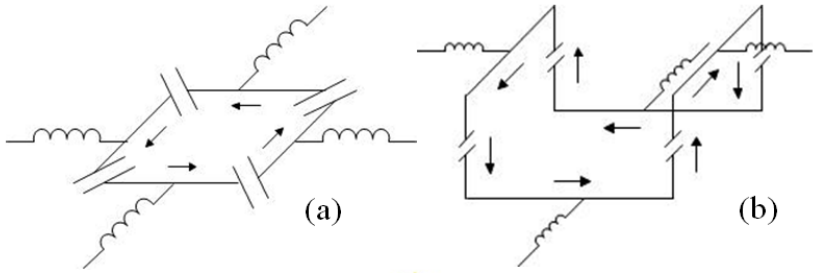

Figure 2.3: (a) uniplanar 2D NRI-TL topology; (b) proposed bi-planar 2D NRI-TL topology (black arrows indicate current directions).

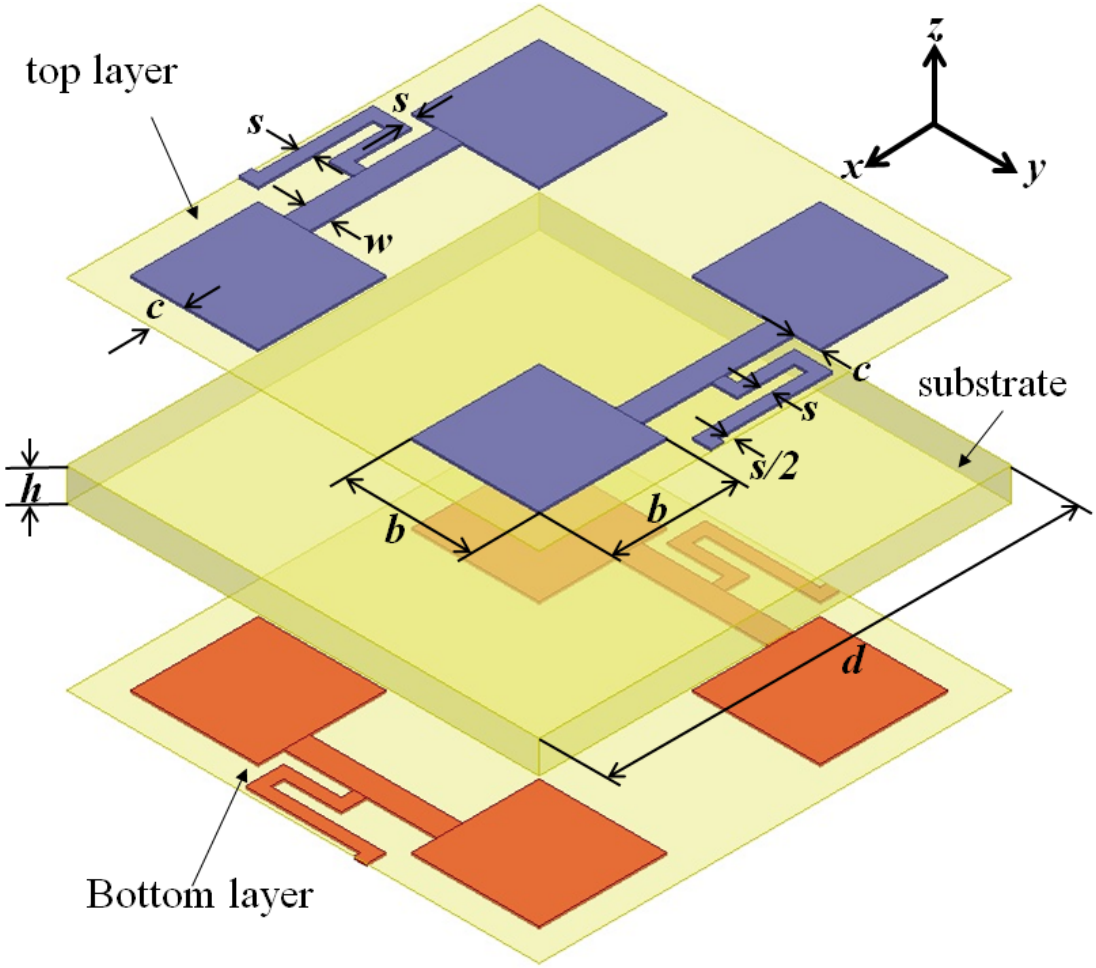

Figure 2.4: An exploded view of a proposed CPS-TL-based implementation using MIM-type capacitors ($d = 3.7\ mm$, $b = 1\ mm$, $c = 0.25\ mm$, $w = 2s = 0.2\ mm$, $h = 0.25\ mm$).

2.1 Representative Design

In this section, a novel bi-planar adaptation of the uniplanar NRI-TL metamaterial layer, as depicted in Figure 2.4, whose reactive loads are distributed across the two metallization layers of a dielectric substrate, is presented. The original uniplanar NRI-TL topology and proposed bi-planar topology are shown in Figure 2.3. Instead of using weak capacitive loads of interdigitated capacitors [35], the proposed design employs MIM-type capacitors, which provide much stronger capacitance, resulting in the lower operating frequencies and smaller electrical size. Additionally, this topology avoids the fine geometric features of the interdigitated capacitors, which contribute to excessive scattering and conductor losses. The Rogers RT/duroid 6010/6010 LM substrate ($\epsilon_r = 10.2, tan\delta = 0.0023$) was chosen as main layers to maximize the capacitance. One main layer was sandwiched by two supporting layers of the same material (Rogers RT/duroid 6010/6010 LM), which were selected to have the same thickness to maximize the NRI bandwidth. The modification of the printed capacitive load leads to major changes in the geometry of the proposed structure as compared with the previous series-node based structure. First of all, the structure becomes bi-planar, as the MIM-type capacitors must be printed on two sides of the substrate. Second, the CPS-TLs along the x and y directions are placed on the top and bottom planes, respectively, as they connect to the capacitors' plates on two different planes, as shown in Figure 2.4. Third, the meandered-line inductors need to be printed on the top and bottom of the substrate as they load to the CPS-TLs. It should be noted that the ring-type currents associated with the NRI response are still evident albeit in biplanar form as shown in Figure 2.3.

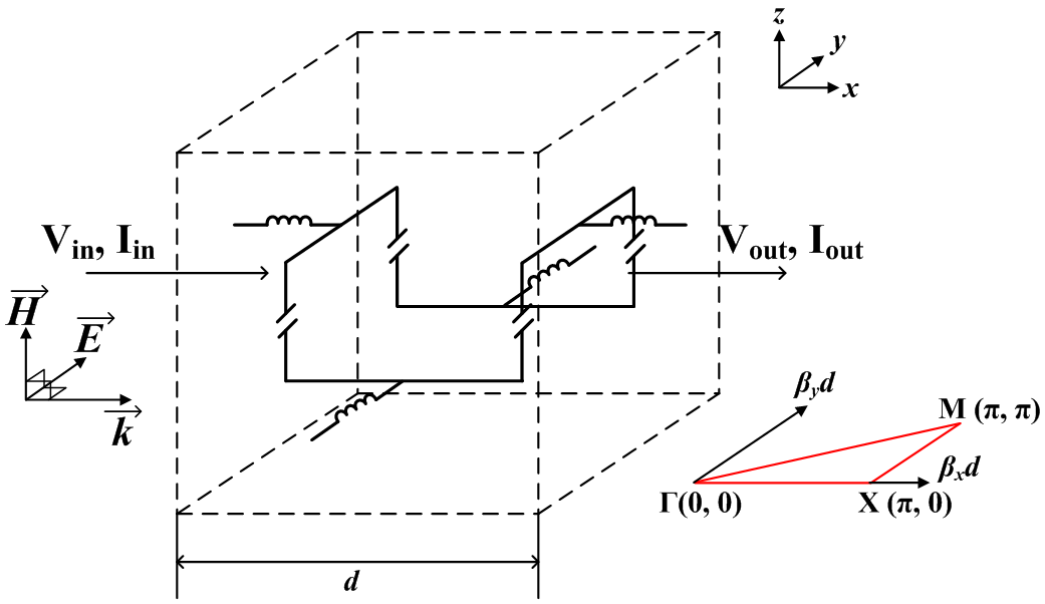

Figure 2.5: The boundaries enclose the representative unit cell.

2.2 Dispersion

The dispersion of a material describes the relationship between the frequency of propagating EM waves and their wavevector. In periodic structures, it suffices to consider the relationship within its irreducible Brillouin zone (the concept is summarized in Appendix.A.I). When considering the normal incidence of the TE-polarized plane wave to the volumetric structure, we only investigate the dispersion along the principal axis, i.e. from Γ to X. Figure 2.5 describes a representative unit cell enclosed by periodic boundaries, which are planes parallel to the xz and xy planes, except for the yz plane because the wave propagates in the x direction. The relationship between the fields at two faces of the unit cell along a certain direction can be represented by Bloch's theorem as

$$\begin{bmatrix} V_{in} \\ I_{in} \end{bmatrix} = \begin{bmatrix} A & B \\ C & D \end{bmatrix} \begin{bmatrix} V_{out} \\ I_{out} \end{bmatrix}, \tag{2.1}$$

$$\begin{bmatrix} V_{out} \\ I_{out} \end{bmatrix} = e^{-j\beta d} \begin{bmatrix} V_{in} \\ I_{in} \end{bmatrix}. \tag{2.2}$$

where d is the length of the unit cell; β is the effective propagation constant of the plane wave within the cell; V_{in}, I_{in} and V_{out}, I_{out} are defined by the input and output fields of the cell, respectively; and the $ABCD$ matrix represents a frequency-dependent operator that transforms the EM fields in terms of voltages and currents from the input to the output. The dispersion relationship of the structure is embedded in the eigenvalue of the equations. Solutions of the equations can be obtained from numerical methods rather than analytical methods, as a closed-form solution is difficult to obtain. As shown in Figure 2.5, the unit cell has periodic boundaries on the planes perpendicular to the y- and z-direction, and the phase shift varies from 0^o to 180^o (or $0 \rightarrow \pi$). It should be noted that the periodic boundary conditions allow waves of both polarizations to propagate in the unit cell, not only the wanted TE-polarized modes. Figure 2.6 shows all the modes of the proposed unit cell up to 10 GHz that satisfy the periodic-phase boundary conditions. The solid blue lines depict the modes for TE polarization, and the dashed red line presents the TM-polarized modes. The TM-polarized modes are normally not excited in reality by free-space TE-polarized plane waves, however, they can exist due to the structure's bianisotropy, although, their magnitude is much weaker that that of the TE-polarized modes. These unwanted modes can be filtered out by replacing the periodic boundaries in the z-direction by magnetic walls and those in the y-direction by electric walls. The dotted lines represent the modes propagating inside the cell when the pe-

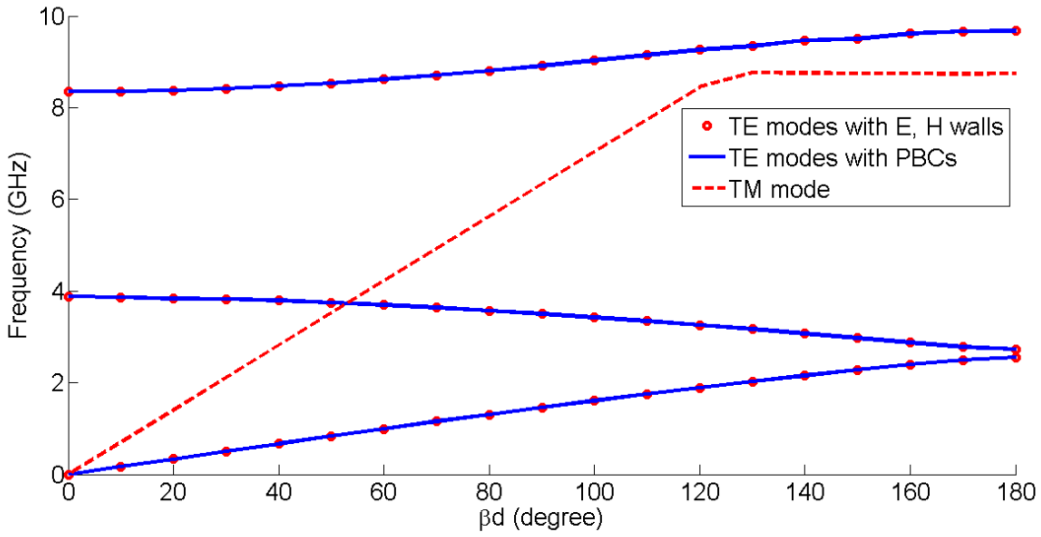

Figure 2.6: Dispersion diagram of the volumetric structure includes both TE- and TM-polarized modes.

riodic boundary conditions are replaced by electric and magnetic walls. The two sets of data show an excellent agreement due to their overlap. Furthermore, the electric and magnetic walls also suggest the periodic boundary condition, because the fields supported by the entire structure can be reconstructed by image theory.

Along with the NRI-loading case with the two types of reactive loads present in the structure, other cases, which remove one or both types of the loads, are studied to investigate the effects of the loaded capacitors and inductors on the structure individually. The capacitive-loading case is formed by eliminating the shunt inductors from the NRI-loading case (Figure 2.7(a)). In Figure 2.7(b), the inductive-loading case is set up from the NRI-loading case by filling the space between the two parallel plates of the capacitors with conducting material to short them. The unloaded case is a superposition of the capacitive-loading and inductive-loading cases, in which the inductors are removed while the capacitors are shorted (Figure 2.7(c)). Figure 2.8(a) displays the dispersion diagram of the capacitive-loading case with a stopband from

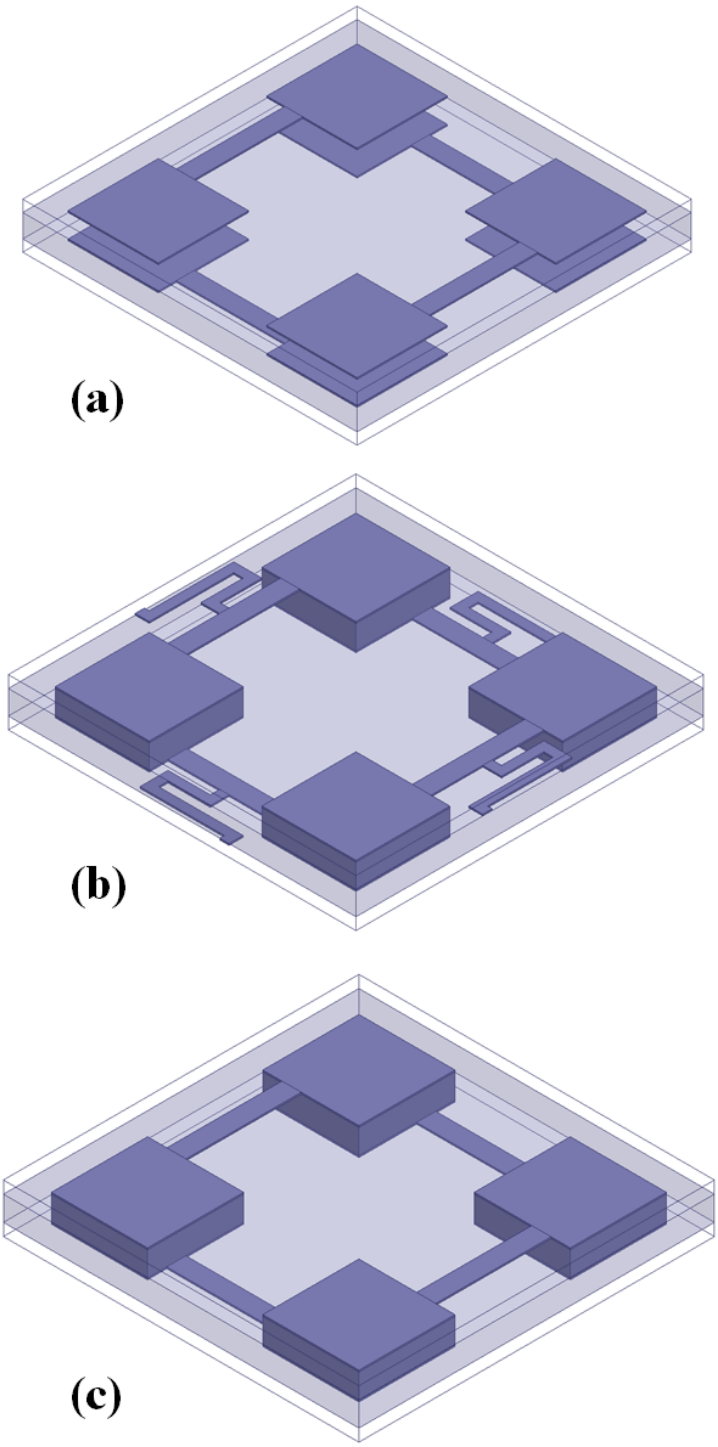

Figure 2.7: (a) Capacitive-loading case; (b) Inductive-loading case, (c) Unloaded case.

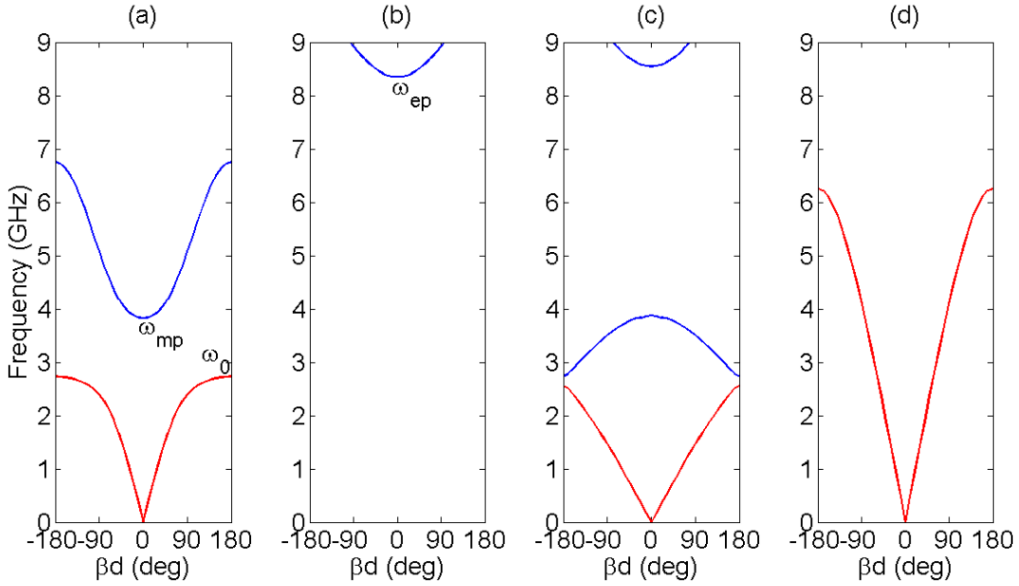

Figure 2.8: Dispersion diagrams for various loading cases: (a) capacitive-only loading, (b) inductive-only loading, (c) capacitive and inductive (NRI) loading, (d) unloaded case.

$\omega_0 = 2\pi \times 2.7\ GHz$ to $\omega_{mp} = 2\pi \times 3.9\ GHz$, corresponding to a region of negative effective permeability [28]. For the inductive-loading case, Figure 2.8(b) shows a stopband below a transition frequency $\omega_{ep} = 2\pi \times 8.3\ GHz$, corresponding to a region of negative effective permittivity. ω_{mp} and ω_{ep} may be considered magnetic and electric plasma frequencies at which the effective medium experiences $\mu_{eff} = 0$ and $\epsilon_{eff} = 0$, respectively. Figure 2.8(c) reveals a passband precisely in the frequency region in which these two responses overlap, where the NRI-loading case exhibits a NRI property. Lastly, the unloaded case presents a typical periodic medium with a linear relationship between its frequency and phase shift at low frequencies and strong dispersion as frequency increases [48].

2.3 Equivalent Circuit Model

In order to capture the behaviors of the volumetric material, an intuitive equivalent circuit model of the structure is proposed using lumped components. The model holds only when the structure meets the effective-medium condition, i.e. its periodicity must be electrically very small. The fully-printed metamaterial in Ref.[35] achieved an electrical length of $\lambda_0/5$, rendering the structure too distributed to model with lumped components [35]. The following model is introduced for a fully-printed version that employs stronger capacitance (MIM-type capacitors) and inductance, resulting in a smaller electrical length. However, as the structure becomes bi-planar in order to accommodate those loads, it produces parasitic effects that should be taken into account.

As seen in the previous section, for TE modes, one unit cell is surrounded by electric and magnetic walls in the directions transverse to the wave propagation, hence, the behaviors of the whole structure resemble those of a parallel plate waveguide (PPW) loaded with one unit cell, shown in Figure 2.9.

The loaded waveguide can be modeled as an equivalent model consisting of one series branch and one shunt branch. The series branch contributes to the waveguide's effective permeability, and the shunt branch contributes to the waveguide's effective permittivity. The series branch includes the intrinsic per-unit-length inductance of the unloaded PPW, which is formulated as $L_{wg}/d_1 = \mu_0 g_{wg} = \mu_0 d_2/p$, where d_1 is the length of the PPW, d_2 is the height of the PPW, and p is the periodicity of the proposed structure in z direction. It should be noted that as the unit cells are square, the length and the height of the PPW are equal to d. When the ring loads to the waveguide, it is excited by the fields inside the PPW, and a current flows along the CPS TLs (along both x and y directions) through the MIM-type capacitors forming a

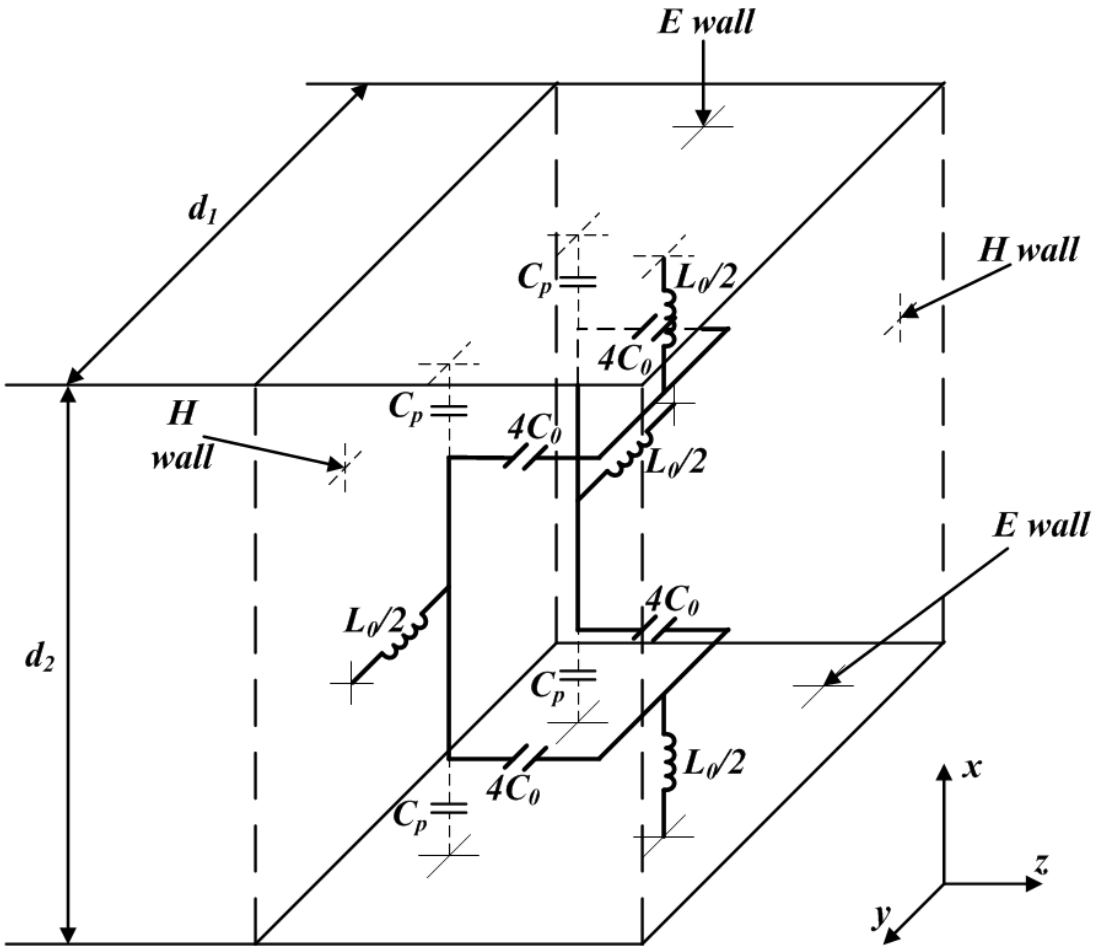

Figure 2.9: A loaded parallel plate waveguide with a NRI-TL unit cell.

loop pattern, as discussed earlier. The capacitively loaded ring, which is represented by a self inductance L_r and total loaded capacitance C_0, behaves similarly as the SRRs, and possesses a magnetic field that interacts with that inside the PPW [4]. As a result, this is accounted for in the model by a mutual coupling inductance formulated as $M = FL_{wg}$, where F is a filling factor, which is the ratio of the total area inside the ring and the area of a unit cell. This inductance describes the broadside coupling between rings through the magnetic walls with the assumption that the edge coupling

between rings is negligible. The shunt branch should first include the intrinsic per-unit-length capacitance of the waveguide ($C_{wg}/d = 2\epsilon_{r2}\epsilon_0 h_2 + \epsilon_{r1}\epsilon_0 h_1$). The current excited by the electric field in the PPW sees the shunt inductive loads (L_0), parasitic capacitance of the CPS ($C_x d$), and the self inductance of the ring reduced by the mutual coupling ($L_r' = L_r - M^2/L_{wg}$). Furthermore, the MIM-type capacitors also create additional capacitors (C_p) between their pads on the bottom layers and the electric walls, as depicted in Figure 2.9. This capacitance is due to the fringing effect between capacitors pads between two adjacent unit cells. A unit cell model with lumped components is introduced in Figure 2.10, and it is further simplified into a series load of $Z'd$ and shunt load of $Y'd$, hence, the effective permeability and permittivity of the metamaterial is expressed as

$$\mu_{eff} = -\frac{jZ'}{\omega g_{wg}}, \tag{2.3}$$

$$\epsilon_{eff} = -\frac{jY' g_{wg}}{\omega}. \tag{2.4}$$

where g_{wg} is the waveguide geometric factor, which accounts for the parallel-plate-waveguide of the transmission line, defined as $g_{wg} = d/p$.

Along with the lumped-component model for the NRI unit cell, the models for capacitive-only loading case, inductive-only loading case, and unloaded case are developed as shown in Figure 2.10. In the inductive-only loading case, the absence of the C_0 can be seen in both the series and shunt branches as the MIM-type capacitors are shorted by filling metal in between their two parallel plates, as shown in Figure 2.10(b). At low frequencies, there is no EM wave propagation due its inductively-shorted shunt branch. The propagation is restored only beyond ω_{ep}, when the capacitive elements dominate as the frequency increases. In Figure 2.10(c), the shunt

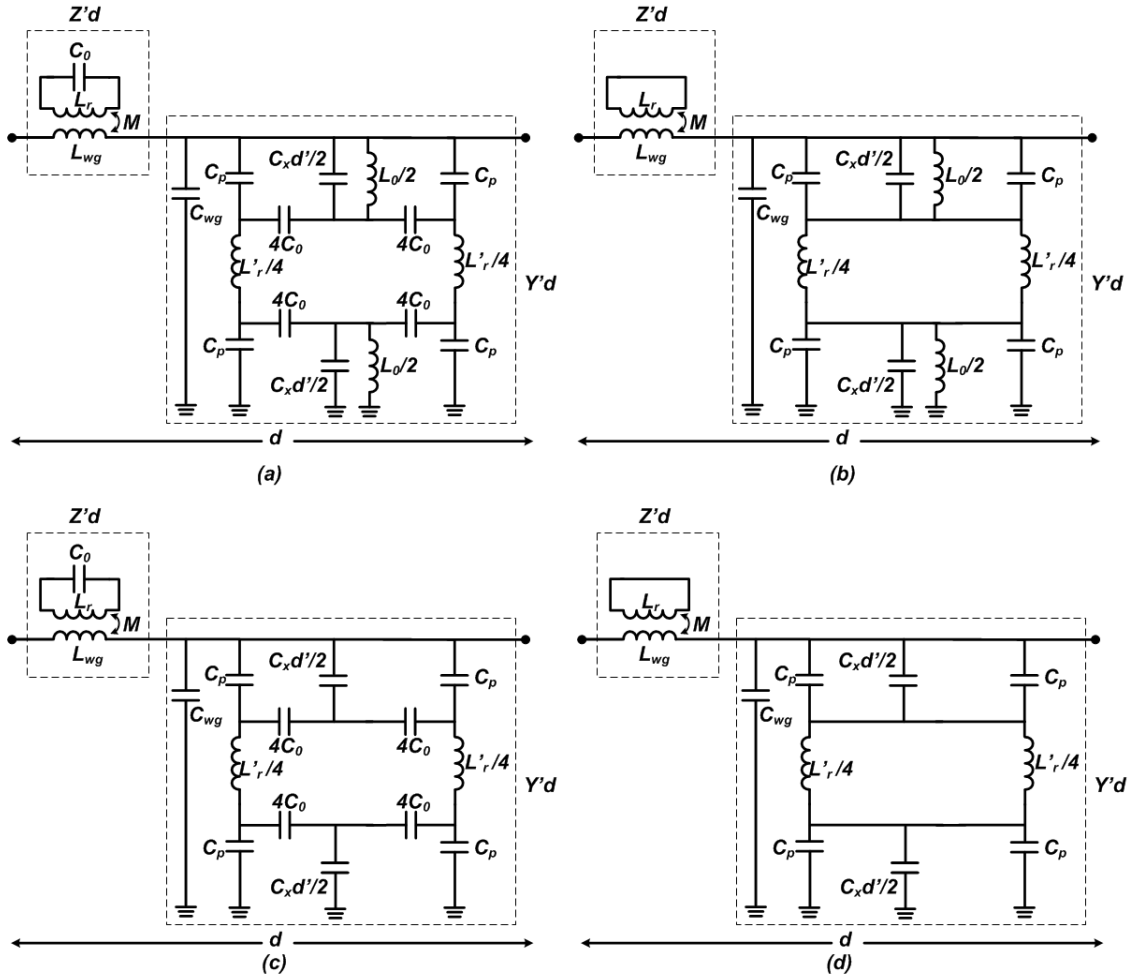

Figure 2.10: Equivalent circuit models of the proposed structure with different loadings: (a) Simultaneously capacitive and inductive loading case or NRI case, (b) Inductive-only loading case, (c) Capacitive-only loading case, (d) unloaded case.

branch of the capacitive-only loading case excludes L_0 due to the removal of the inductive loads. The structure supports wave propagation at low frequencies because of the inductive series branch. As the frequency rises, the $L_r - C_0$ ring resonates at ω_0, rendering the series branch capacitive and resulting in a stop band. The EM waves begin to propagate again when the capacitive load C_0 resonates with the series inductance of the waveguide, which is reduced by the mutual coupling, L_r' at the fre-

quency of ω_{mp}. In the final case, the shunt and series branches omit both capacitive and inductive loads (C_0 and L_0) as shown in Figure 2.10(d).

2.4 Effective-Parameter Retrieval

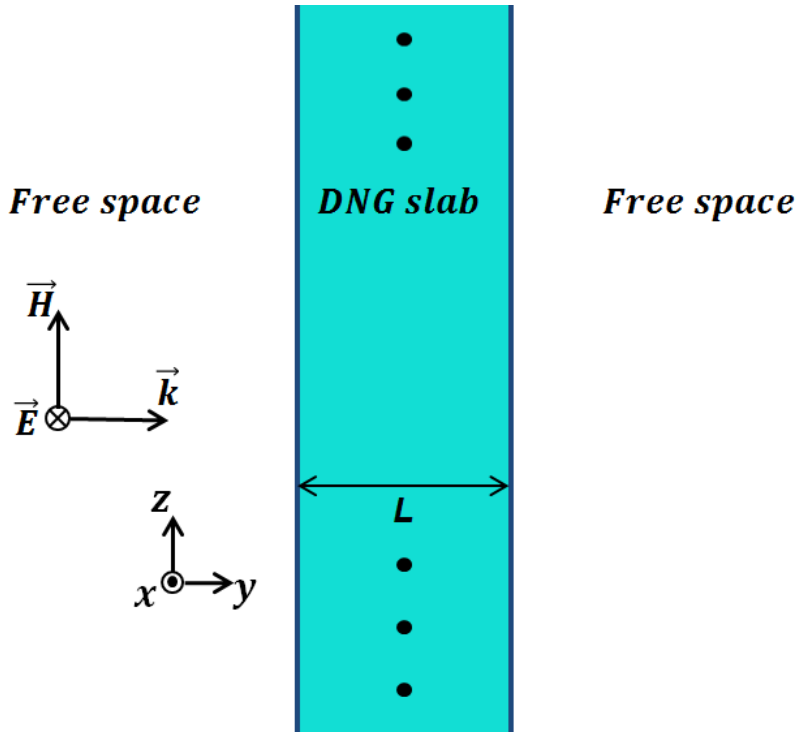

Figure 2.11: A TE plane wave incident normally on a DNG slab of thickness L.

Now that the metamaterial is considered an effective medium, its effective permittivity and permeability can be retrieved from the scattering data. Recall that the permittivity and permeability can be calculated directly from the index of refraction n and impedance z as $\epsilon = n/z$, and $\mu = nz$. Assume that a normally incident plane wave from free space hits a slab of metamaterial (DNG), which is infinite in the x and z directions, and has a thickness L, as shown in Figure 2.11. The scattering parameters of the slab are represented in terms of n and z as [21, 49]

$$S_{11} = \frac{R(1 - e^{j2nkL})}{1 - R^2 e^{j2nkL}}, \tag{2.5}$$

$$S_{21} = \frac{(1 - R^2)e^{j2nkL}}{1 - R^2 e^{j2nkL}}. \tag{2.6}$$

where $R = (z - 1)/(z + 1)$, and k is the wavenumber of the plane wave in free space. Once the S-parameters are measured, the impedance z and the refractive index n can be obtained from

$$z = \pm\sqrt{\frac{(1 + S_{11})^2 - S_{21}^2}{(1 - S_{11})^2 - S_{21}^2}}, \tag{2.7}$$

$$n = \frac{1}{kL}[Im\{\ln(e^{jnkL})\} + 2m\pi] - jRe\{\ln(e^{jnkL})\}. \tag{2.8}$$

where L is the length of the slab, and m is an integer. In equation 2.7, the sign is chosen so that $z' \geq 0$ as the metamaterial is a passive medium. Because of periodic nature of the exponential function, there are multiple values of m that satisfy equation 2.8, however, there is only one values ensure the continuity of the effective refractive index n. The selection of the branch index m must ensure the continuity of the curve n'. This extraction procedure will be applied for the designed structure to obtain its effective permittivity and permeability in the following chapter.

Chapter 3

Design and Simulation

3.1 Design

The representative design presented in previous chapter exhibited a NRI over the range between 2.7 GHz and 3.9 GHz. Although the structure possessed simultaneous negative permittivity and permeability in the NRI band, the dispersion of the ENG case showed that its permittivity is obtained only at very high frequency. This leads to large negative permittivity in the NRI band, which complicates the design for free-space matching. From this, it could be surmised that the meandered-line inductance was extremely weak. The extraction procedure, which is introduced later in the chapter, yielded an extracted inductance of around 1 nH over the frequencies of interest, affirming the above conclusion. As the loading inductors were printed in the small gaps (0.9 mm) between the CPS lines, their inductance was inevitably low because a meandered-line inductor's length is limited and is not able to obtain sufficiently large inductance. Increasing the gap size for accommodating more meandered lines is not an option to overcome this shortcoming, since the unit cell was designed to be compact. Furthermore, the capacitors occupied a substantial area of the unit

cell, resulting in potential parasitic effects, which might be difficult to be modelled in the equivalent circuit. Therefore, the modified design needs to build upon the previous design in order to attain better free-space matching, and accuracy of the equivalent-circuit model. However, as a compromise, the electrical length of the new structure will increase.

The exploded view of the optimized design's unit cell is introduced in Figure.3.1, which is modified relative to the representative design. The modifications involve the unit-cell dimensions, the host TLs, the dielectric layers, and the loading elements. The design procedure, which employs knowledge gained from the equivalent-circuit model, is presented in the following sections. Unlike the design with discrete elements, in which the value of the loads is explicitly calculated from the model, the design process for fully printed loads employs the equivalent-circuit model to predict the trend of the proposed structure, implicitly find the loading values of capacitors and inductors, and then representing them as printed components.

3.1.1 Unit Cell Redesign

The demand to obtain stronger loading inductance requires the enlargement of the unit cell. The new unit-cell dimension is selected to be $6.2\ mm \times 6.2\ mm$, guaranteeing an acceptable electrical length of $\lambda_0/11$ for an operation frequency near $4.4\ GHz$. It should be noted that the MIM-type capacitors provide strong enough capacitance to obtain a permeability-plasma frequency much lower than $4.4\ GHz$. However, a commensurate permittivity plasma frequency using inductors, printed with a standard lithography process, is difficult, if not impossible, to obtain at lower than that frequency.

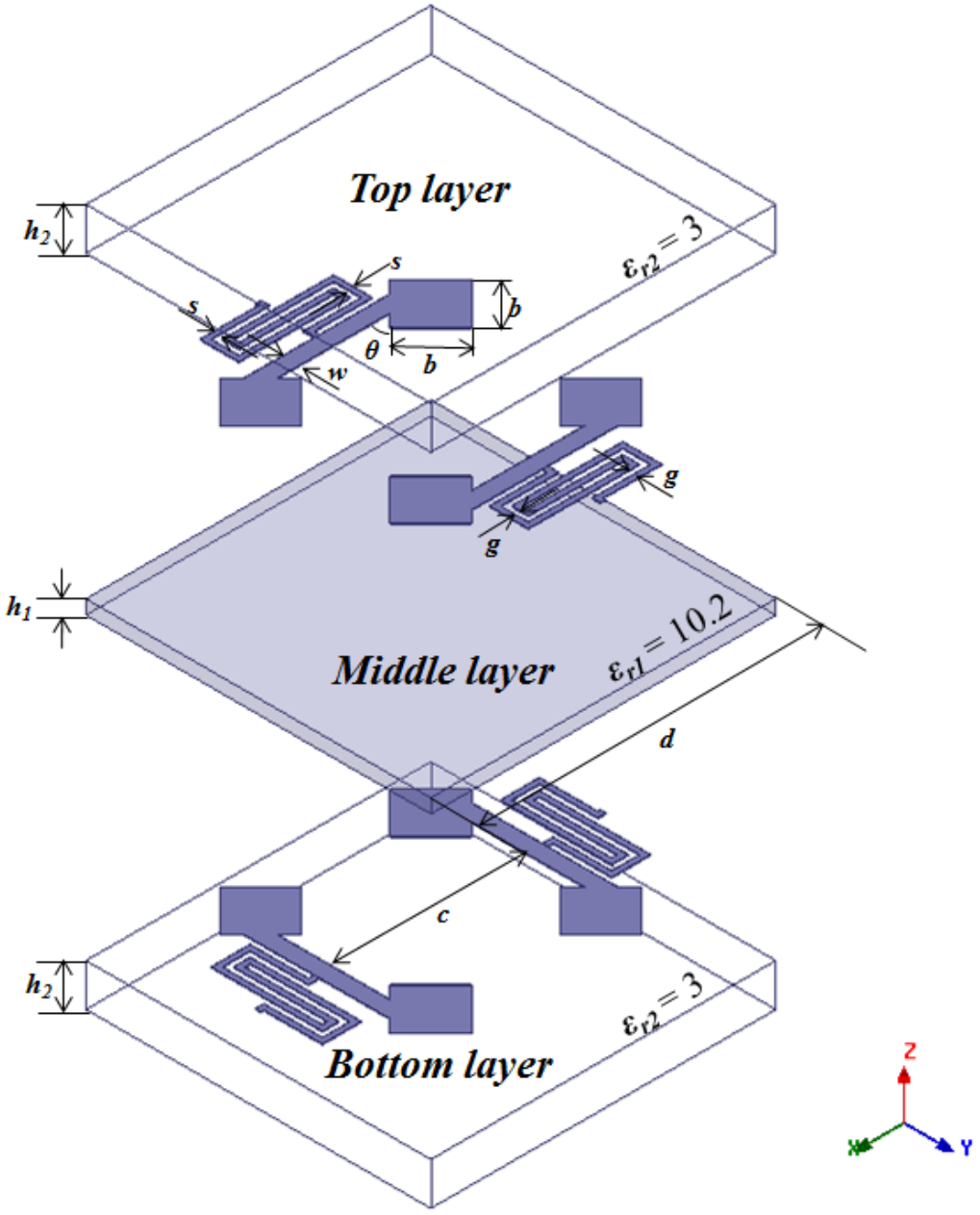

Figure 3.1: An exploded view of the fully-printed NRI-TL metamaterial unit cell using MIM-type capacitors and dual-arm spiral inductors as series and shunt loads, respectively.

3.1.2 CPS Design

The ratio between the area surrounded by the CPS lines and that of the unit cell defines the filling factor, F, which is proportional to the NRI bandwidth. To this end, the CPS lines are adjusted to enclose a considerable area in the unit cell. However, the CPS lines cannot be placed at the very edge of the unit cell because there will be not much room left for the printed inductors. As a trade-off, the CPS TLs are chosen to have a gap of 2.1 mm, for which the distance from the unit-cell edge to CPS rings is 1.05 mm.

3.1.3 Dielectric Layers

The modified design still consists of three layers, in which the fields are concentrated in the middle layer, as in the previous design. The middle layer of thickness h_1, as portrayed in Figure 3.2(a), is the dielectric layer between the two parallel capacitor plates, predominantly contributing to the loading capacitance. The same material in the representative design, Rogers RT/duroid 6010/6010 LM, is utilized in the modified design. The material has a high dielectric constant of $\epsilon_r = 10.2$ and a low loss tangent of $tan\delta = 0.0023$ [50].

The extension of the unit-cell size creates an increase in the total inductance ($L_{wg} = \mu_0 d^2/p$) of the PPW as the electric walls are pushed farther from each other, i.e. as d increases. This reduces the effective inductance ($L'_r = L_r - F^2 L_{wg}$) of the ring, hence, raising the ω_{m0}, and narrowing the MNG and NRI bandwidth. It is worth mentioning that the total inductance of the PPW varies with the unit cell's vertical period p. Additionally, the two supporting layers of the representative design, whose thicknesses are 10 mil, are too thin, making the structure too flexible, and therefore easy to bend. Hence, to provide more rigidity to the new design, new layers of

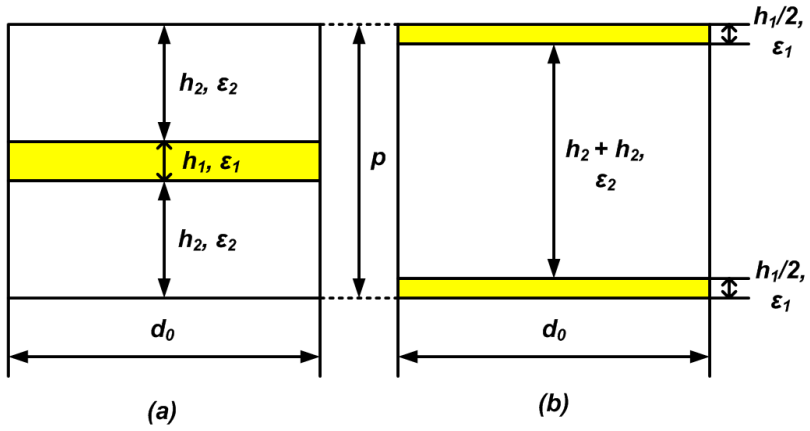

Figure 3.2: Vertical view of a unit cell: (a) the main layer in the middle; (b) the unit cell moved half a period in the vertical direction.

$h_2 = 30\ mil$ height are used to substitute these layers. If we view the unit cell by shifting its center a half of its period in the vertical direction (i.e., by $p/2$), the new perspective shows the two adjacent supporting layers as a $2h_2 = 60\ mil$ substrate sandwiched by two $h_1/2 = 5\ mil$ layers, as depicted in Figure.3.2(b). To this extent, the structure can be easily fabricated by stacking 10 mil layers and 60 mil layers alternately.

Once the gap between the main layers is incremented, the total capacitance ($C_{wg} = \epsilon_0\epsilon_{r1}h_1 + 2\epsilon_0\epsilon_{r2}h_2$) of the PPW rises, which results in an increase in permittivity's plasma frequency as the inductive loads resonate with the incremented shunt capacitance at a higher frequency. The frequency can be maintained by choosing the supporting substrate to be Rogers RO 3003, whose dielectric constant ϵ_r is 3, and loss tangent $tan\delta$ is 0.0013 [51]. As a comparison to the representative design, the thickness h_2 is tripled, but the supporting layer's dielectric constant ϵ_{r2} decreases by more than 3 times, so that the intrinsic capacitance of the PPW is almost unchanged. The advantages of this solution are to provide more rigidity to the structure; to confine the fields to the main layer, which has high dielectric constant and is thinner

than other layers; and to maintain the PPW's intrinsic inductance and capacitance of the representative design, whose behaviour is already known.

The Table 3.1 presents a parametric study of the effects of the main-layer thickness on the negative-permeability band. The capacitor plate dimension is selected as $1\ mm \times 1\ mm$, the two supporting layers possess a thickness of 30 mil, and the height of the substrate varies according to standard, commercially available thicknesses [50].

TABLE 3.1: **Variation of negative permeability band with substrate thickness**

No.	h_1 **(mil)**	ω_{mp} $(\times 10^9)(rad/s)$	**BW (GHz)**	**Fractional BW (%)**
1	50	$2\pi \times 7.84$	1.56	22
2	25	$2\pi \times 6.43$	1.07	18.15
3	10	$2\pi \times 4.68$	0.68	15.68
4	5	$2\pi \times 3.32$	0.21	10

As shown in Table 3.1, the structure's magnetic plasma frequency can be shifted down by decreasing the thickness of the main layer, although the bandwidth of the MNG region also shrinks. The 10 mil substrate is selected as a compromise between the electrical length and the fractional bandwidth, for transverse unit-cell dimensions of $6.2\ mm \times 6.2\ mm$.

3.1.4 MIM-Type Capcitors

The MIM-type capacitors employed in the structure have parallel square plates, hence, their capacitance is roughly estimated as follows

$$C_0 = \frac{\epsilon_0 \epsilon_{r1} b^2}{h_1} \tag{3.1}$$

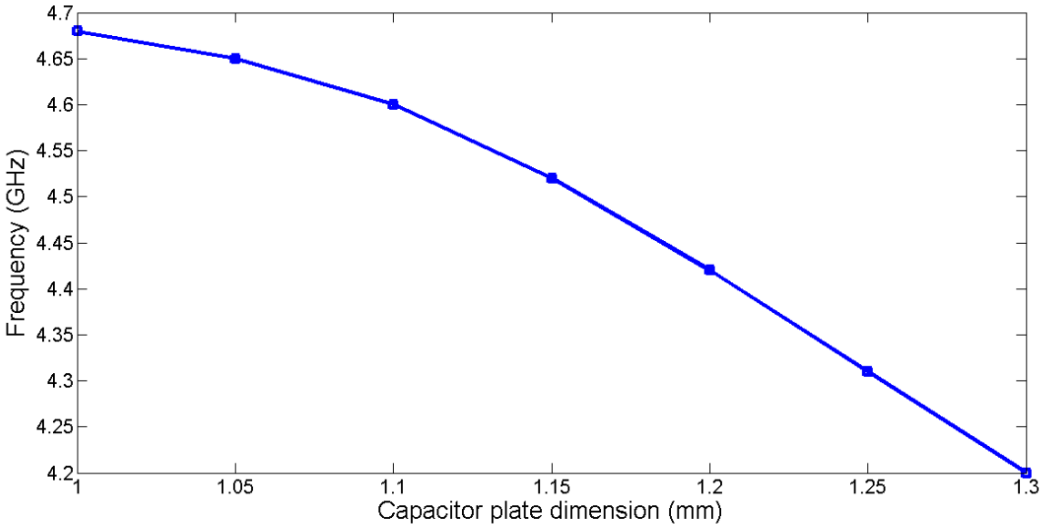

Figure 3.3: Dependence of the permeability plasma frequency on the dimension of the loading MIM-type capacitors' square plates.

where b is the linear dimension of the square plates, and ϵ_{r1} and h_1 are relative permittivity and thickness of the main layer, respectively. In the preceding discussion, we already selected the material for the substrate as well as its thickness. The only parameter left to design is the dimension of the parallel plates. In the representative design, the plates of 1 $mm \times 1$ mm were chosen for the series capacitive loads. The dimension could have been selected to be larger, rendering a lower plasma frequency of the structure's effective permeability; however, as the total area of the plates occupied a great amount of the unit-cell area, their broad size reduced the filling factors, causing a reduction in the bandwidth, and creating unwanted coupling between closely placed capacitors. The new extended unit cell is able to accommodate bigger plates of the loading MIM-type capacitors. The relationship between the MNG point and the size of the MIM-type capacitors, which ranges from 1 mm to 1.3 mm is shown in Figure 3.3.

Figure 3.3 displays the range of the structure's permeability plasma frequency

from 4.2 GHz to 4.68 GHz. As the printed inductor does not provide many options for loading inductance due to the geometric constraints, the data show that MIM-type capacitors offer more freedom for design. In addition, the MIM-type capacitors in the new design are rotated by an angle of 45^o in order to mitigate the coupling between the parallel plates in adjacent unit cells.

3.1.5 Printed Inductors

The use of meandered-line inductors could not provide adequate inductance to shift down ω_{ep} to a lower range. As the inductance of a meandered-line inductor is proportional to its meandered length, a large value of inductance requires a large area to accommodate the meander, which expands the periodicity of the unit cell. Spiral inductors could be an option that produces stronger inductance although occupying a similar area. However, the fabrication of spiral inductors demands air bridges, rendering them complicated and costly. The presented design proposes the use of dual-arm spiral inductors, which have higher inductance than meandered-line inductors but do not need air bridges. The loading inductors are allocated a gap of 2.1 mm between a pair of CPS conductors. In order to maximize the length and number of turns of the inductors, the width and the gap of the metal strip are pushed to the fabrication limit of 0.1 mm for conventional lithography processes ($s = g = 0.1$ mm). The designed inductor consists of two smaller dual-arm inductors in series, as shown in Figure 3.4. It is reasonable to suggest that if only one dual-arm spiral inductor is created in the same area, it can be longer, and have more turns, leading to larger inductance. However, in the assumption stated in Chapter 2, an E-wall is imposed at the middle of the gap, shorting all the turns of the spiral inductor, therefore, two smaller dual-arm spiral inductors are needed to properly satisfy the boundary condition.

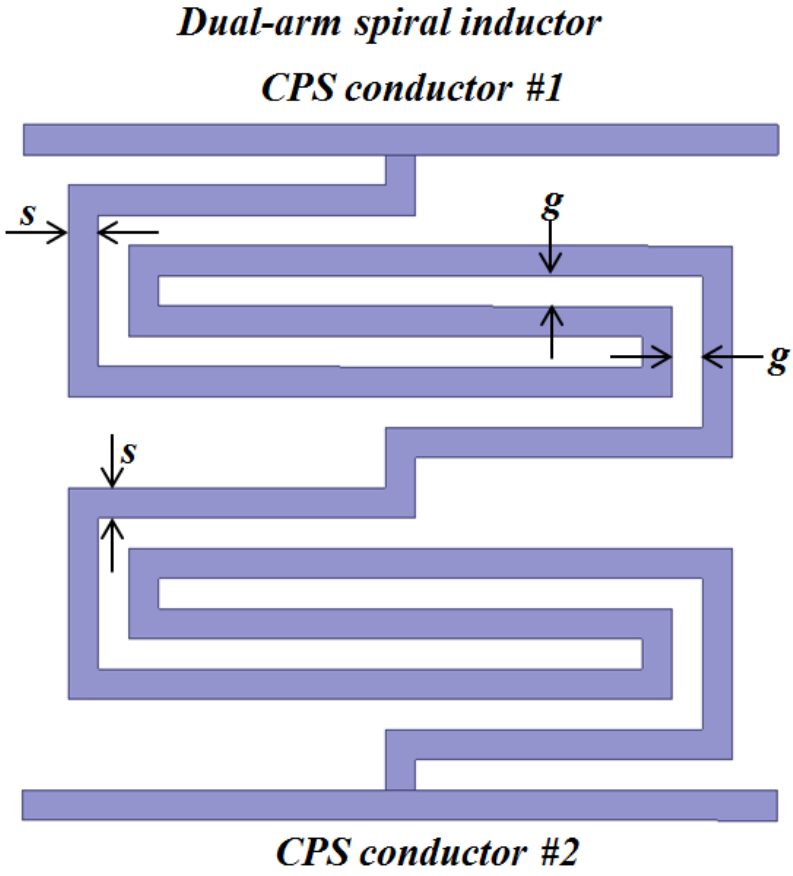

Figure 3.4: Implementation of a dual-arm spiral inductor in the gap between two CPS lines.

To investigate the inductance of the designed inductors, the dual-arm spiral inductor is loaded to a CPS TL in shunt fashion, as shown in Figure 3.4. Full-wave simulations using HFSS's driven modal solver were performed, in which the ports were referenced to the centre of the inductor to collect scattering parameters of the inductor. A T-model was then employed to extract the equivalent inductance in a regime ranging from low frequencies to those just above the inductor's resonance. Figure 3.5 describes the equivalent inductance and the real part (or the resistive loss) of the dual-arm spiral inductor; while the inset represents the equivalent circuit model for the designed inductor. The equivalent inductance is related to the length and arrangement of the continuous metal strip; as previously noted, the longer the strip, the larger the inductance. The equivalent resistor is attributed to the conductor loss and surface roughness of the strip. The capacitor in the equivalent circuit represents the total capacitance of the gap among the strips in the spiral inductor. As more turns are created, the inductor's length is increased, and more gaps are created, resulting in the rise of both equivalent inductance and parasitic capacitance, and a downshift of the self-resonance frequency.

As shown in the Figure 3.5a, the dual-arm spiral inductor obtains a pretty high inductance of 7 nH at 4.4 GHz, and remains relatively constant over the range of interest. Of course, the self-resonance frequency should be as far as possible from this range to reduce losses. In this case, the self-resonant frequency is at 6.8 GHz.

Although the printed inductors are the main factor that decides the negative-permittivity region of the structure, in the equivalent-circuit model, the parasitic capacitance of the CPS TL, which is in shunt with these inductors, also contributes to the behaviour of the shunt branch. The following study inquires into the relationship between the width of CPS TL and the plasma frequency of permittivity. It should be noted that the inductors, which are investigated above, are loaded in shunt to the

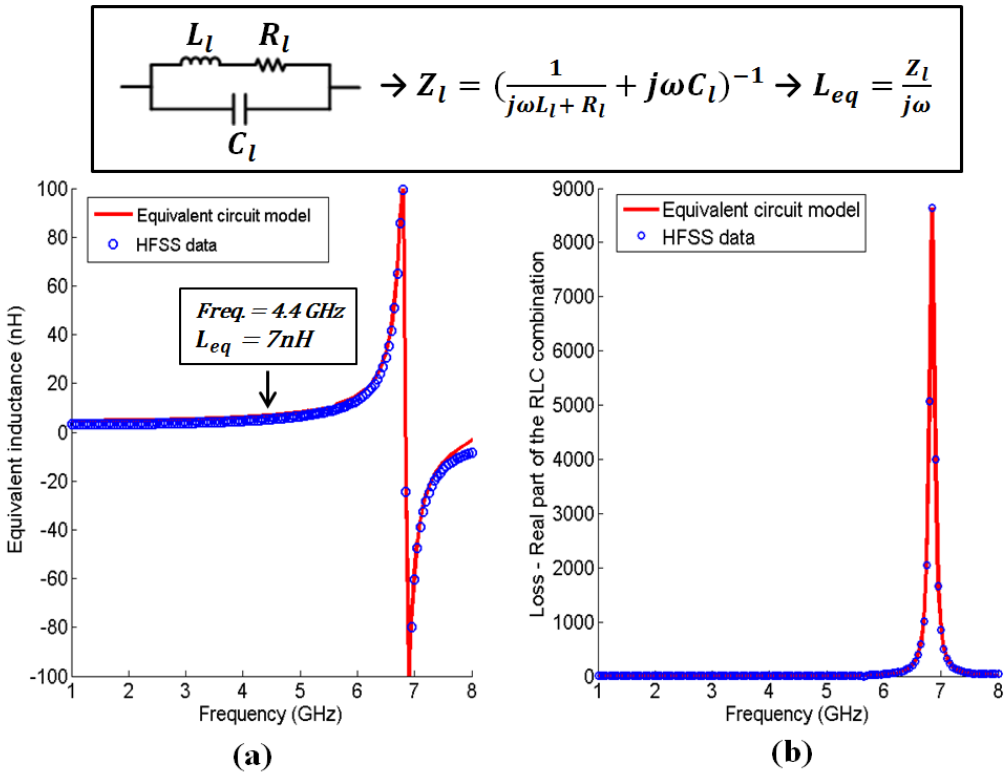

Figure 3.5: (a) Equivalent inductance ($Re\{L_{eq}\}$); (b) Real part of RLC circuit impedance or loss ($Re\{Z_l\}$).

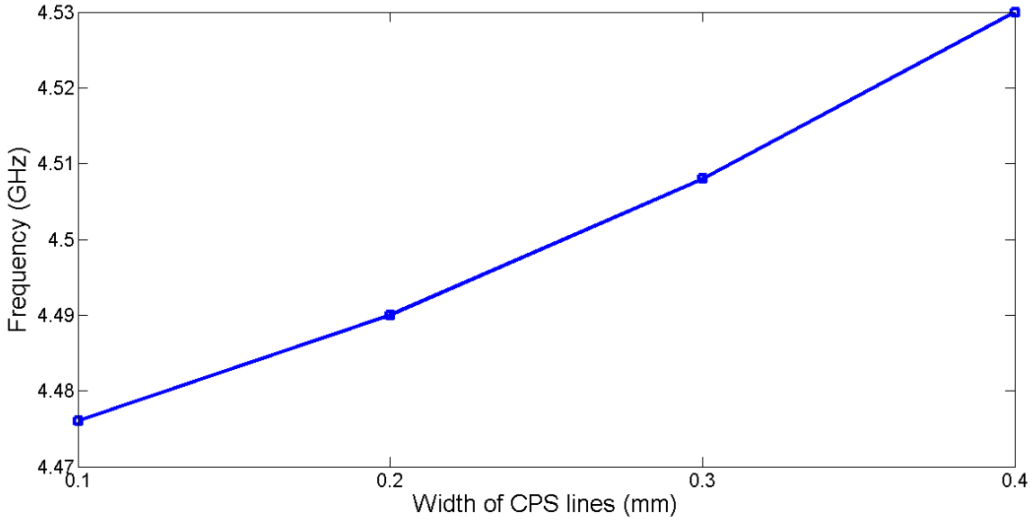

Figure 3.6: Dependence of the permittivity plasma frequency on the width of the CPS conductors.

CPS TL.

Figure 3.6 shows that ω_{ep} increases as the width of CPS TL rises, which implies that the performance of the loading inductance is compromised by the increase in the conductor's width. It is attributed to the fact that the parasitic capacitance of the CPS TL, which is proportional to the CPS width, offsets the dual-arm spiral inductors that are in shunt with it. Although the plasma frequency is only marginally dependent on the CPS width, this relationship can be exploited as an alternate way to manipulate the negative region of permittivity when the modification of the loading inductors is complicated by geometric constraints.

3.2 Simulations

3.2.1 Dispersion Simulations

As mentioned in the preceding chapter, the dispersion properties of the proposed structure, or the dependence of wavenumber on frequency in an infinitely periodic medium, are obtained from full-wave simulation using Ansys's High Frequency Structure Simulator's (HFSS's) eigenmode solver. The proposed structure's eigenmode simulation setup is presented in Figure 3.7. The main consideration is the propagation of TE waves, which have their magnetic field normal to the structure's plane, along one axis, for example along the y direction in this case, so that Master/Slave (M/S) boundaries are imposed on faces perpendicular to the propagation direction (y), and the phase shift between these two faces varies from 0^o to 180^o. The faces that are normal to the z direction are assigned as magnetic walls or M/S boundaries with zero phase shift. Similarly, the faces perpendicular to the x direction are assigned as electric walls or M/S boundaries without phase shift.

3.2.2 Transmission Simulations

Transmission simulations are used to measure the degree of free-space matching for the proposed structure. HFSS simulates the normal incidence of a plane wave excited from free space to a transversely infinite and finitely thick slab of the designed metamaterial. The scattering parameters, which are referenced to the interfaces between free space and the slab, are collected to assess the matching and the loss of the slab. Furthermore, these parameters can be utilized to extract the effective permittivity and permeability of the slab, provided that its unit-cell dimension is small enough to meet the effective-medium condition.

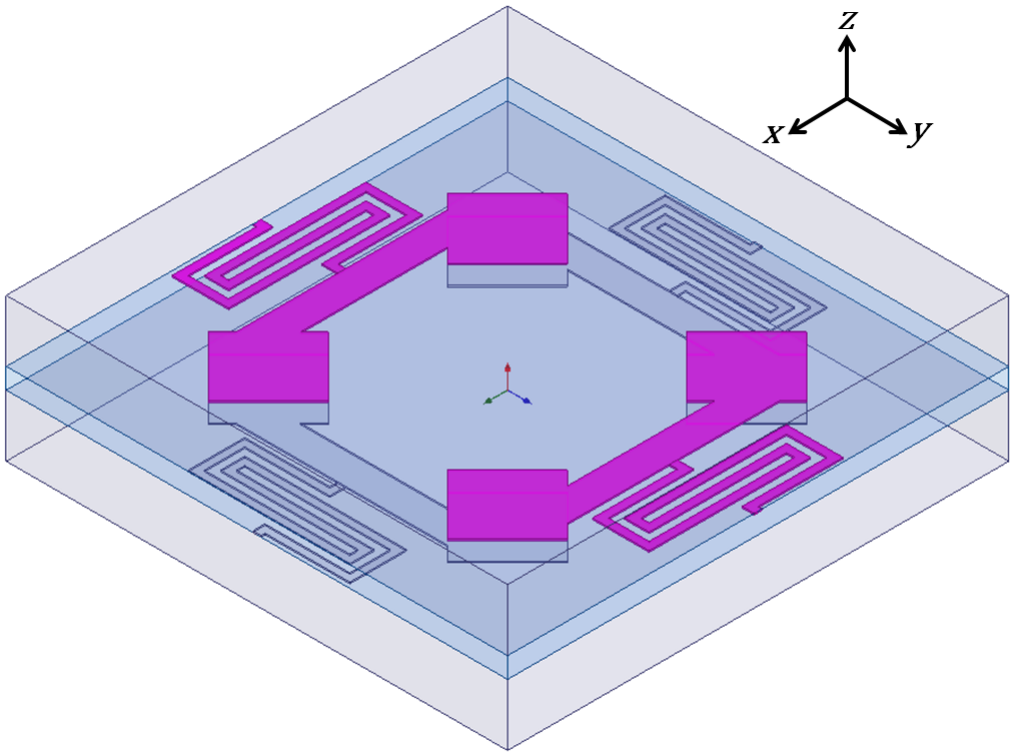

Figure 3.7: The eigenmode simulation setup in HFSS used to investigate the dispersion properties of the structure.

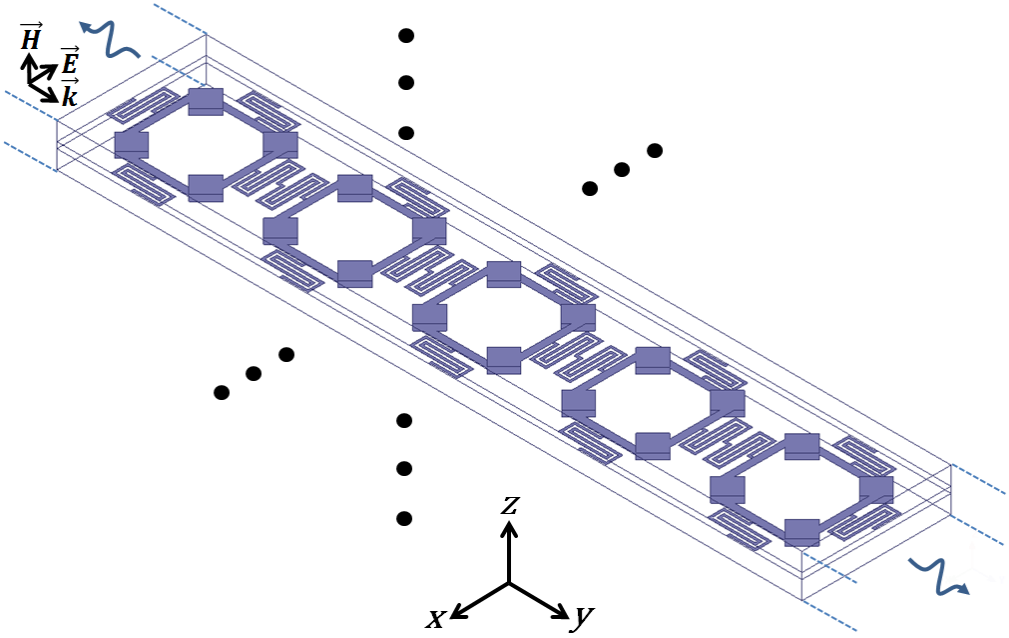

Figure 3.8: The transmission simulation of the transversely infinite and 5-unit-cell thick metamaterial slab collecting scattering parameters at the interfaces of the slab and free space.

Figure 3.8 describes the simulation of the 5-unit-cell thick and transversely infinite slab consisting of designed unit cells. The planes on the top and bottom of the slab are assigned zero-phase-shift M/S boundaries or magnetic walls. Similarly, the faces normal to x direction are assigned M/S boundary conditions with zero phase shift or electric walls. The plane wave is excited from free space, and propagates in y direction with vertically polarized $\overrightarrow{H}$ and horizontally polarized $\overrightarrow{E}$. The metal used is copper ($\sigma = 5.8 \times 10^7\ S/m$) with finite thickness $t_c = 17\ \mu m$, surface roughness of $0.5\ \mu m$.

3.2.3 Optimization and Results

As mentioned earlier, free-space matching can be obtained when the effective relative permittivity and permeability are simultaneously equal to negative unity. The results from Section 3.1 report that the plasma frequency of permeability varies from $4.2\ GHz$ to $4.68\ GHz$, while that of permittivity ranges from $4.48\ GHz$ to $4.53\ GHz$, thus the two plasma frequency ranges overlap. This suggests that we should conduct a parametric study of both the width of CPS TL and the size of the MIM-type capacitor's parallel plates to search for the combination that produces the best matching.

Figure 3.9 exhibits the intersection of the metamaterial structure's NRI mode and the light line, the latter of which represents the dispersion of an EM wave travelling in free space. At this frequency, the NRI mode and the free-space EM wave have equal phase velocities of opposite sign, suggesting that the structure has a refractive index of -1. If the structure also has low reflection at this frequency, it means that the structure is matched to free space with $\epsilon_{eff} = \mu_{eff} = -1$ [36]. The optimization is conducted in two steps:

1. Find the phase matching point from the dispersion diagram,

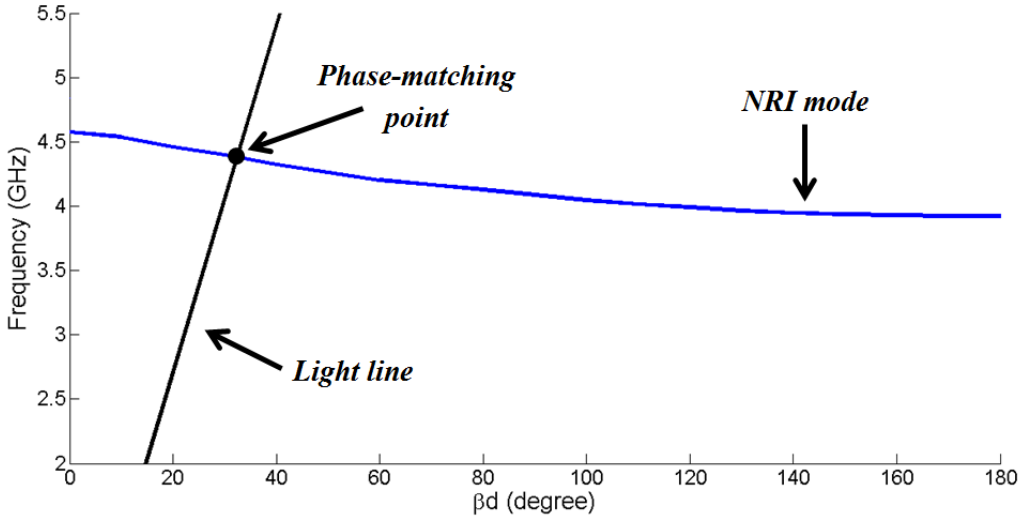

Figure 3.9: Typical dispersion of a volumetric NRI-TL metamaterial: the light line intersects the NRI mode at the phase-matching point.

2. Collect the scattering parameters at the phase-matching frequency.

Figure 3.10 shows the scattering parameters, S_{11} and S_{21}, of a 5-unit-cell long slab of the designed metamaterial for different combinations of the CPS width and the capacitor's plate length at their respective phase matching points. For the 0.2 mm CPS width, the structure suffers from a serious mismatch for all plate dimensions. At CPS width of 0.3 mm and 0.4 mm, there are two cases that provide good free-space matching and are significant in comparison with the others: 0.3 mm CPS width, 1 $mm \times 1$ mm plate, and 0.4 mm CPS width, 1.05 $mm \times 1.05$ mm plate. The former possesses a return loss of 17.35 dB, and an insertion loss of 1.4 $dB/unitcell$, while the latter has a 19.97 dB return loss, and a 1.5 dB/unit-cell insertion loss. These two cases may be regarded as equal with respect to performance, and the latter is selected for further investigation. All the dimensions of the design are listed in Table 3.2.

The dispersion properties of the final design are investigated for 4 cases: (a) Un-

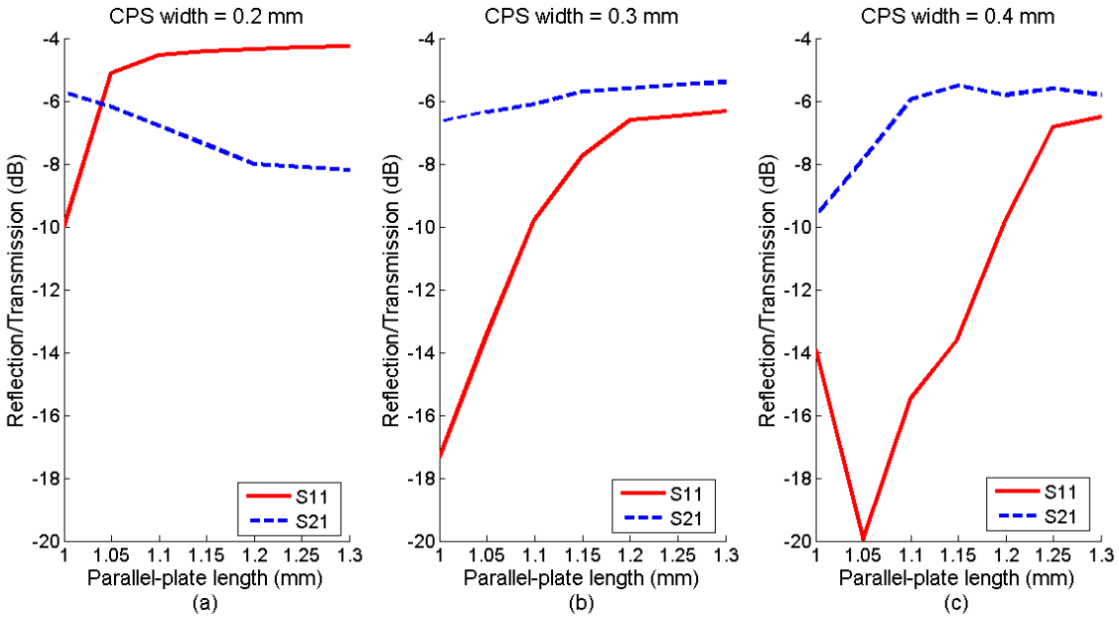

Figure 3.10: The reflection and transmission at the phase-matching point as the CPS width and MIM-type capacitor's plate length vary: (a) CPS width = 0.2 mm; (b) CPS width = 0.3 mm; (c) CPS width = 0.4 mm.

loaded case; (b) Inductively-loaded case; (c) Capacitively-loaded case; (d) NRI-loaded case. As shown in Figure 3.11, the NRI band in the NRI loading case coincides with the stopband produced by negative permeability in the capacitive-only loading case, i.e. $\omega_{m0} = \omega_0 = 2\pi \times 3.92\ GHz$ and $\omega_{mp} = \omega_{c2} = 2\pi \times 4.57\ GHz$. This corresponds to a fractional NRI bandwidth of 15.3%. There is a small stopband between ω_{c2} and ω_{c1} which corresponds to the region of positive permeability and negative permittivity, and the propagation resumes for frequencies above $\omega_{c1} = 2\pi \times 4.8\ GHz$. Other than a small discrepancy, the plasma frequency of permittivity in the inductively-loaded case is close to ω_{c1} in the NRI loading case. Small differences may be attributed to the fact that the metal-filled capacitors' considerable dimension adds extra inductance to the shunt loads. Furthermore, the equivalent-circuit model introduced in Section 2.3 can capture the same dispersion data as those from eigenmode simulations for both cases.

TABLE 3.2: **Design parameters for one unit cell**

Quantity	**Symbol**	**Value**
Main-layer thickness	h_1	10 mil
Main-layer dielectric constant	ϵ_{r1}	10.2
Supporting-layer thickness	h_2	30 mil
Supporting-layer dielectric constant	ϵ_{r2}	3
Periodicity	d	6.2 mm
CPS width	w	0.4 mm
CPS gap	$d-w-c$	2.1 mm
Capacitor plate rotation angle	θ	45^o
Capacitor plate length	b	1.05 mm
Inductor strip width	s	0.1 mm
Inductor strip gap	g	0.1 mm

Figure 3.11 depicts the agreement between the two sets of data in the region where the effective-medium condition is valid, i.e. $\beta d \leq \pi/4$. Because the printed inductors are characterized in the previous section, the inductive loads are substituted as an equivalent RLC circuit (R_l, C_l, L_l). The elements in the equivalent circuit models are summarized in Table 3.3.

Besides the simulation of the 5-unit-cell thick slab, another simulation of the 3-unit-cell thick slab is conducted. Apart from the purpose of investigating the structure's reflection and transmission over a certain range of frequencies, such simulations ensure the accuracy and reliability of the effective-parameter extraction as well. The 3-unit-cell-slab simulation is carried out as a supplement to the 5-unit-cell-slab simulation in order to avoid data misinterpretation due to resonances, particularly Fabry-

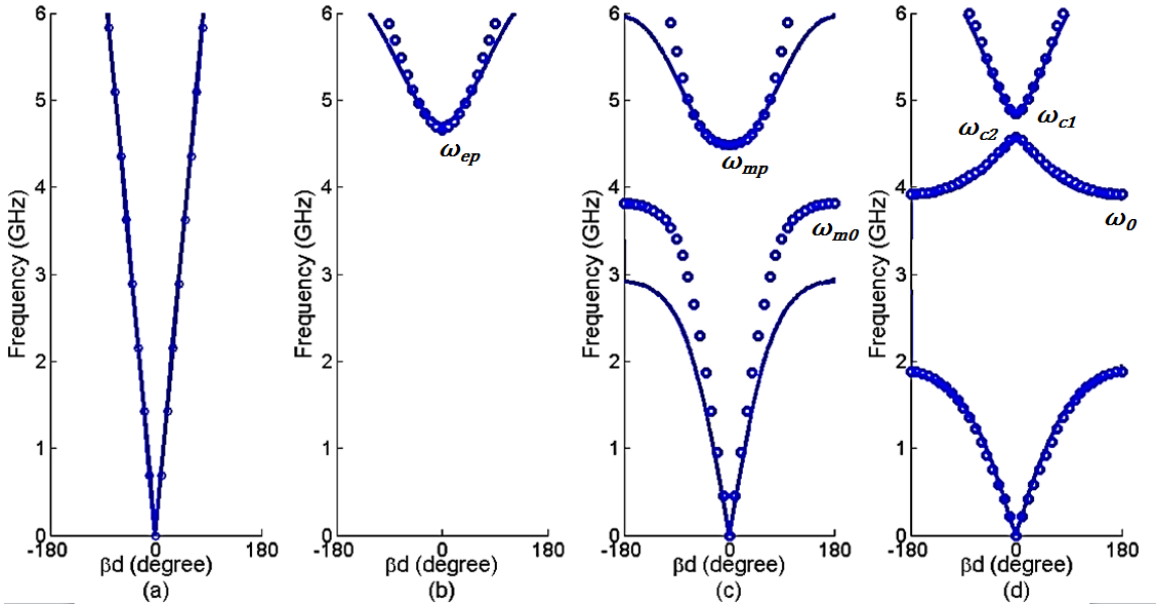

Figure 3.11: Dispersion diagram of the final design in 4 cases: (a) Unloaded case; (b) Inductive-only loading case; (c) Capacitive-only loading case; (d) NRI loading case. The solid lines represents the simulated data, whereas the dotted lines are those from equivalent circuit models

Perot resonances. The scattering parameters of the slab consisting of the proposed structure for different thicknesses are displayed in Figure 3.12 and Figure 3.13.

Figure 3.13 displays a return loss of 13.34 dB and an insertion loss of 1.5 $dB/unitcell$ at 4.4 GHz, affirming the 5-unit-cell-slab results. Both data also agree in the extraction of effective permittivity and permeability, shown in Figure 3.14. When the effective parameter retrieval introduced in Chapter 2 is applied to these transmission data, the real parts of effective permittivity and effective permeability are obtained as $Re(\epsilon_{eff}) = -0.89$ ($\Delta\epsilon = 0.11$) and $Re(\mu_{eff}) = -1.08$ ($\Delta\mu = 0.08$), respectively, and both are close to -1 at 4.4 GHz ($\Delta f_\epsilon = 0.025\ GHz$, $\Delta f_\mu = 0.015\ GHz$). The imaginary parts of these parameters are $Im(\epsilon_{eff}) = 0.5$ and $Im(\mu_{eff}) = 0.09$. These values show that the structure is lossy, hence its resolution is severely degraded. The losses, which are mainly embedded in the effective permittivity, suggest that the in-

TABLE 3.3: **Values of lumped elements in the equivalent circuit models**

Element	Symbol	Value
Loading capacitor	C_0	0.128 pF
Equivalent shunt loading inductor	L_l	2.841 nH
Equivalent shunt loading capacitor	C_l	0.23 pF
Equivalent shunt loading resistor	R_l	1.74 Ω
Parasitic capacitance	C_p	0.0128 pF
Ring inductance	L_r	17.12 nH
Filling factor	F	0.53 mm

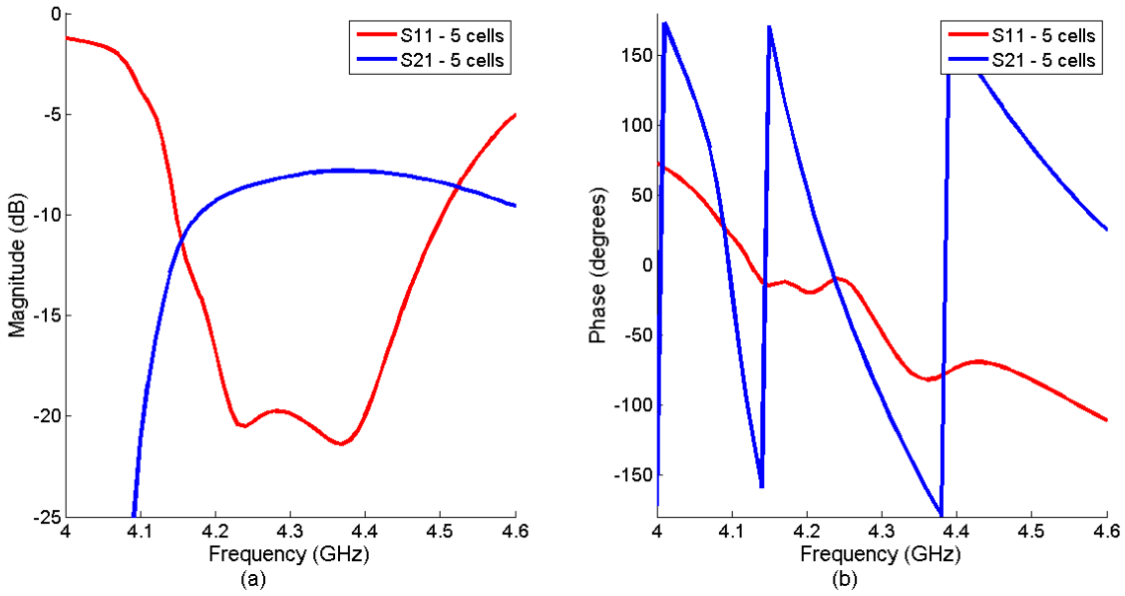

Figure 3.12: Reflection and transmission properties of the transversely infinite and 5-unit-cell thick volumetric NRI-TL metamaterial slab : (a) Magnitude; (b) Phase.

ductive loads are the major source. This agrees with the fact that the resistor R_l in the dual-arm spiral inductor's RLC model is large.

The homogeneity of the structure at 4.4 GHz is verified by an eigenmode simula-

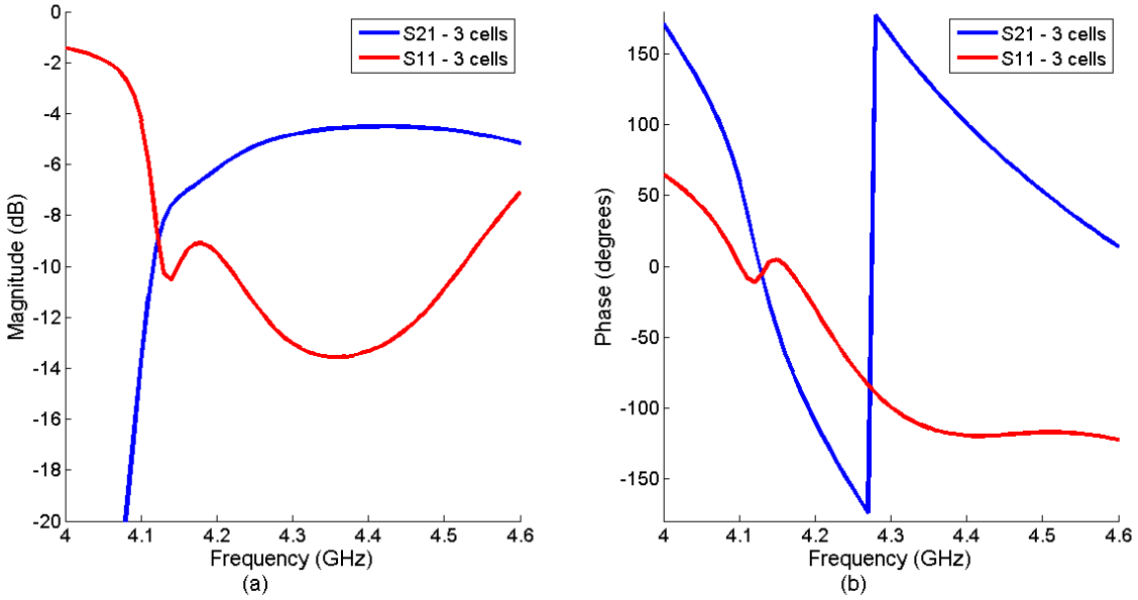

Figure 3.13: Reflection and transmission properties of the transversely infinite and 3-unit-cell thick volumetric NRI-TL metamaterial slab : (a) Magnitude; (b) Phase.

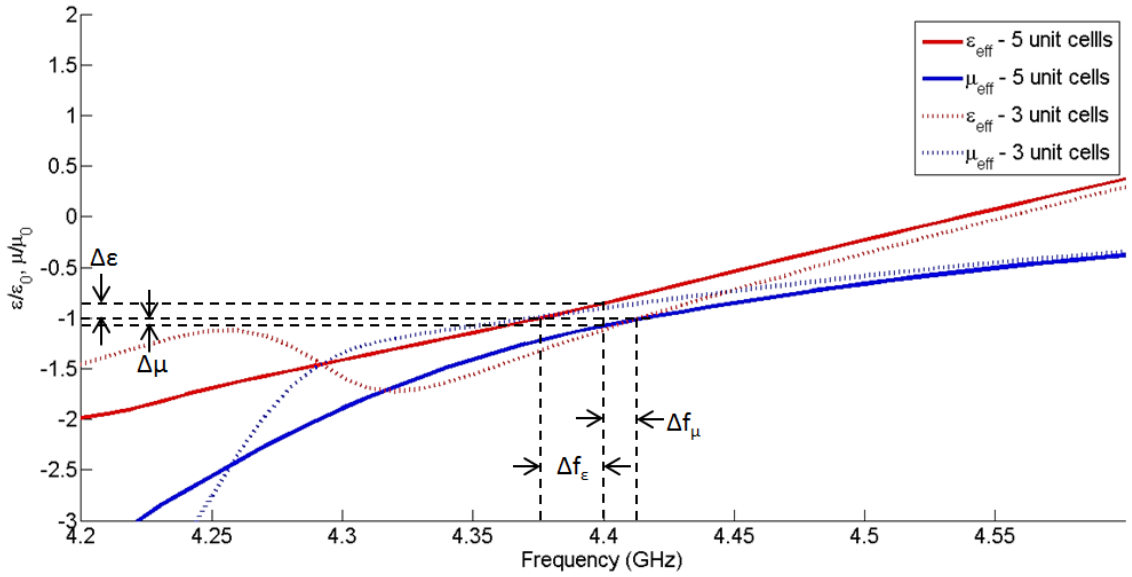

Figure 3.14: The extracted effective permittivity and permeability of the 3-unit-cell and 5-unit-cell thick slabs.

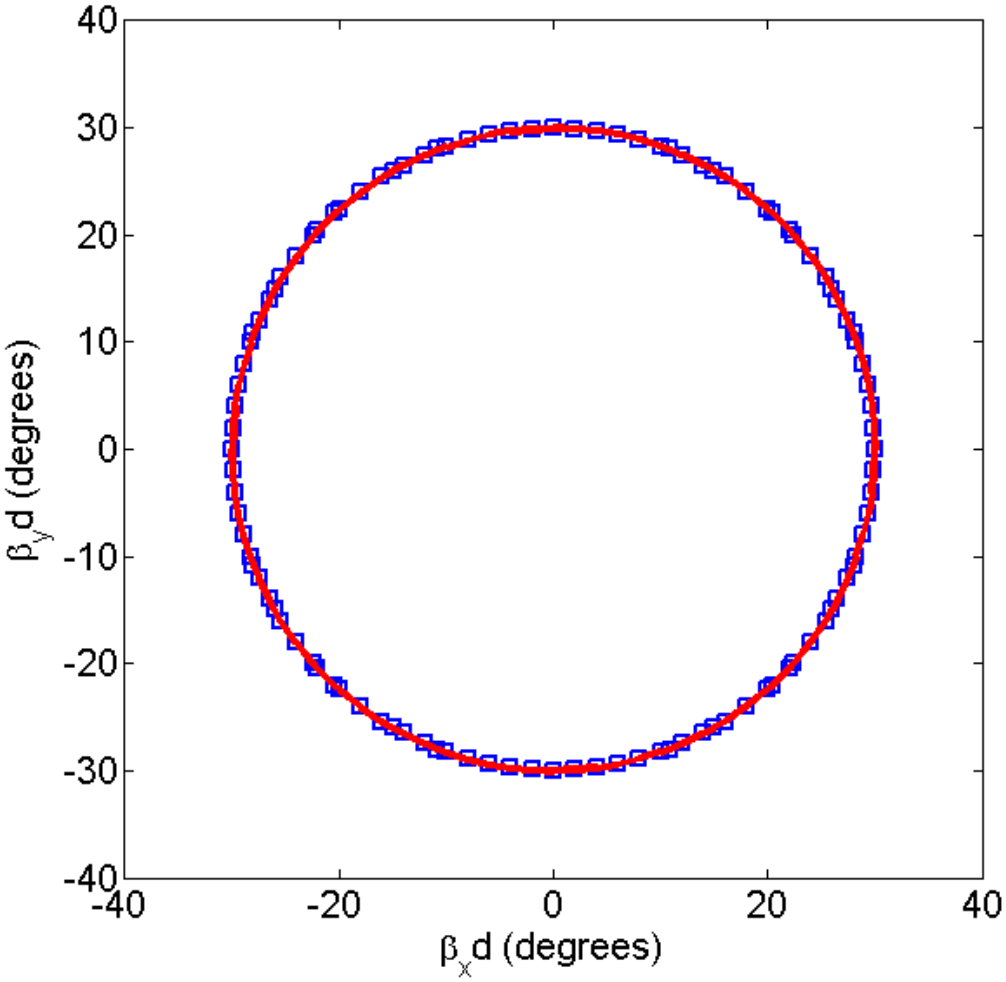

Figure 3.15: At 4.4 GHz the equifrequency contour (blue-square circle) of the proposed volumetric NRI-TL metamaterial overlaps that (red solid line) of the EM wave propagates in free space.

tion, in which both the phase shifts in the x and y direction vary. The equifrequency contour at 4.4 GHz shows the near coincidence of the propagation from all directions on the material plane, and overlaps the equifrequency of the EM-wave propagation in free space, as shown in Figure 3.15. Therefore, the designed NRI-TL metamaterial is nearly isotropic at this frequency. The fabrication and the measurement setup of the metamaterial are presented in the following chapter.

Chapter 4

Experiment Setup and Procedure

4.1 Fabrication

The fabrication of the volumetric NRI-TL metamaterial began with the chemical etching of the designed patterns on both sides of a Rogers RO3003 substrate, which has relative permittivity of $\epsilon_{r2} = 3$, thickness of 60 mil (1.524 mm), and clad-copper thickness of 0.5 oz (17 mm), shown in Figure 4.1(a). The copper layer on each board has gold cladding to minimize the effect of surface roughness and resistivity on the performance of the volumetric metamaterial. As mentioned in the previous chapter, these Rogers RO3003 layers are stacked alternately with de-metallized 10 mil Rogers RT6010 ($\epsilon_{r1} = 10.2$) as in Figure 4.1. The 60 mil Rogers RO3003 substrate is used, because the material is widely prevalent in manufacturing of printed-circuit boards, thus, reducing the cost. The fabricated board has a width of 18.6 mm, equal to the dimension of 3 unit cells, a length of 142.6 mm, consisting of the 80.6 mm, or 13-unit-cell, long patterned portion located at the centre of the board, and two blank, 5-unit-cell long portions on either side used for aligning purposes. The layers of Rogers RT6010 are cut to have the same dimensions as the Rogers RO3003 layers.

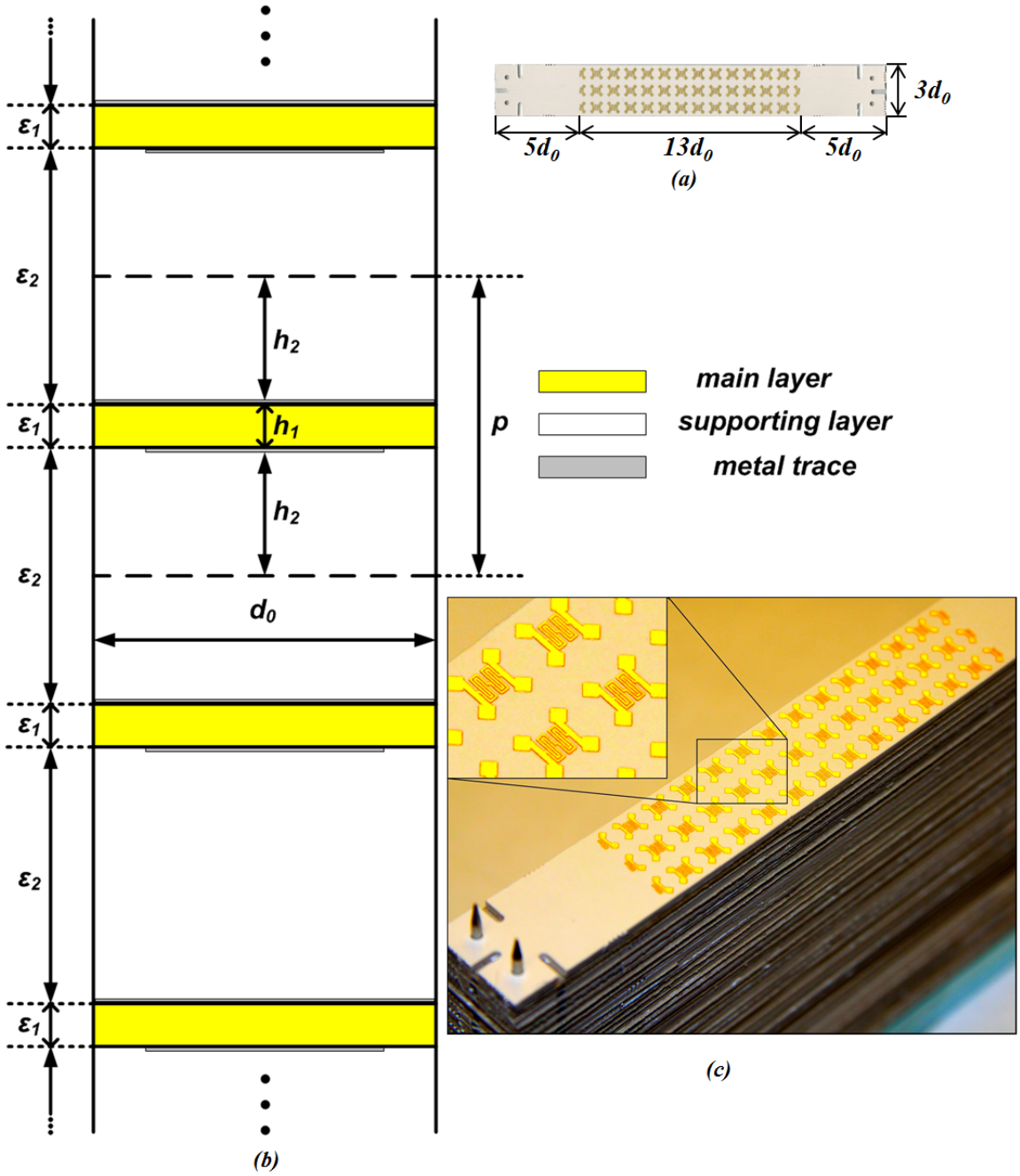

Figure 4.1: Fabrication of the volumetric NRI-TL metamaterial: (a) one board of Rogers RO3003 printed with the design pattern; (b) a schematic view of stacking 10 *mil* Rogers RT6010 and 60 *mil* Rogers RO3003 alternately; (c) the assembling of the layers in progress, the inset is a zoom-in view of the NRI-TL pattern.

These layers are stacked alternately, and are aligned by putting four stainless steel pins through the holes drilled at four corners of each board, displayed in Figure 4.1(b), (c). The fully constructed volumetric NRI-TL metamaterial consists of 46 boards of Rogers RO3003 and 45 layers of Rogers RT6010, resulting in its height of 8.18 *cm*. Although the structure contains four pins inside, the electromagnetic field is confined into the central part of the slab away from the pins. Furthermore, the excited electric field is perpendicular to the pins, so that it does not stimulate current to flow along them.

4.2 Measurement Setup

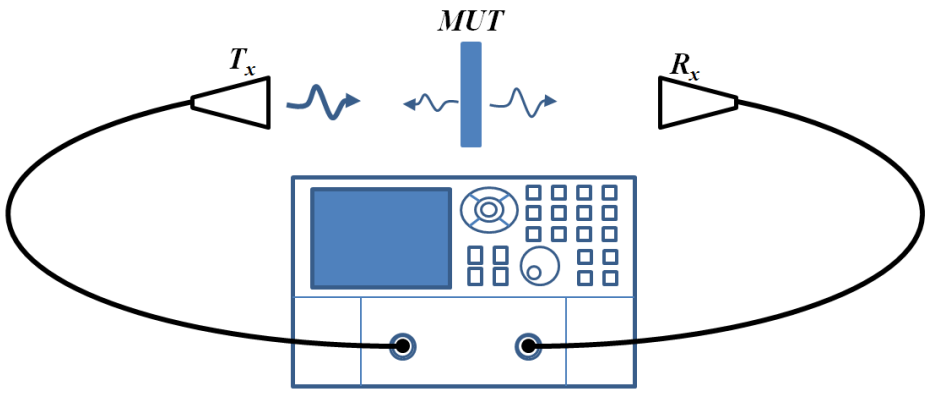

Figure 4.2: A schematic of the free-space transmission method.

Measurements are performed on the constructed volumetric NRI-TL metamaterial and its effective permittivity and permeability are extracted to determine the NRI-TL's interaction with electromagnetic waves excited from free space. There are several techniques for measuring dielectric properties of a material sample such as the perturbation method, waveguide and coaxial transmission-line method, resonators and transmission-line method, and free-space transmission method, to name

a few. Although each method has its own advantages in different measurement contexts, the free-space transmission method appears to be the most appropriate method in this experiment, where the material under test (MUT) is a flat-parallel faced slab, because this method measures how the MUT as a flat lens interacts with a free-space source with suitable polarization. In addition, it is a non-contacting, non-destructive method.

This method requires a system consisting of a vector network analyzer, and two standard gain horn (SGH) antennas facing each other with a sample held between them, as shown in Figure 4.2. In the experiment, the free-space system employs an Agilent Performance Network Analyzer (PNA) E8362B, ranging from 10 MHz to 20 GHz, and two 15 dBi SGH (waveguide size $WR-187$) antennas operating from 3.95 GHz to 5.85 GHz. In order to be outside the reactive region of the two SGH antennas, the distance between the antennas and MUT must be greater than $2d^2/\lambda$, where d is the largest dimension of the SGH antenna aperture, and λ is the wavelength of the frequency of interest. Moreover, the MUT should have a known thickness, which is large enough ($L > \lambda/18$) for the scattering parameters to be measurable, but should not exceed one wavelength to avoid multiple roots in the extraction procedure. After the MUT is measured for its transmission and reflection properties, the measured data are utilized to extract the MUT's effective permittivity and permeability.

To improve the illumination of the SGH antennas, the antenna field is concentrated into a Gaussian-like beam whose waist is small enough to lie within the slab face to minimize the diffraction at MUT's edges by lenses. Without the lenses, the MUT should be surrounded by absorbers to prevent extraneous components from reaching the receiving antenna without propagating through the sample. Two metallic lenses are utilized to transform the antenna's field to a plane wave at the transmitting side,

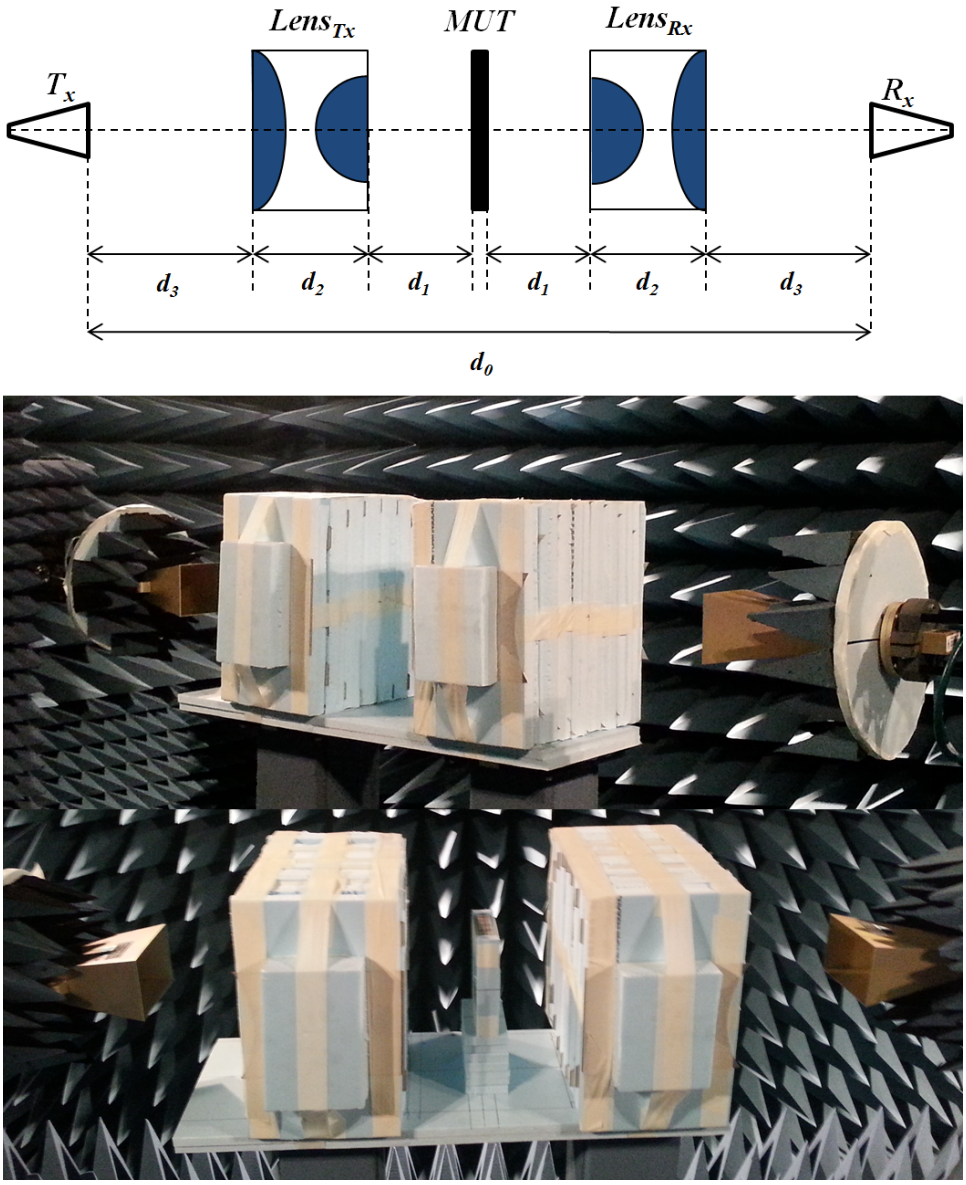

Figure 4.3: Scheme of the experimental setup (top), and the actual arrangement inside an anechoic chamber (bottom).

and vice versa at the receiving end. The details of design and fabrication of these two lenses are introduced in Appendix A.II. The plane waves produced by the lenses have electric field parallel to their metal plates, hence, the volumetric NRI-TL slab was rotated by 90^o in order to receive proper excitation. The placement of lenses,

MUT, and SGH antennas with details of position ($d_0 = 106.94\ cm, d_1 = 10.9\ cm, d_2 = 20\ cm, d_3 = 21.64\ cm$).

4.3 Calibration Technique

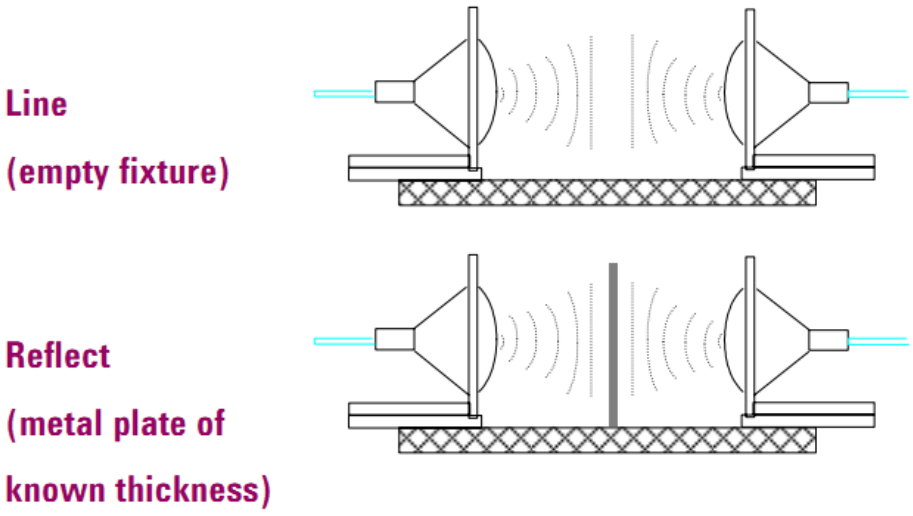

Figure 4.4: Fixtures of GRL calibration: (top) line/empty, (bottom) reflect standard [52].

The metallic lenses were already built, and experiments were conducted inside an anechoic chamber, as displayed in Figure 4.3. Before the free-space transmission measurements are conducted, a calibration process must be performed to remove systematic errors. The most frequently used calibration techniques are Through Reflect Match (TRM), Through Reflect Line (TRL), and Gated Reflect Line (GRL). TRM and TRL methods are frequency-domain calibration techniques that collect scattering parameters from known cases to determine the error coefficients. However, the GRL method was selected because it does not require broad-band absorbers or high-precision positioning fixtures, which are not yet available in the lab.

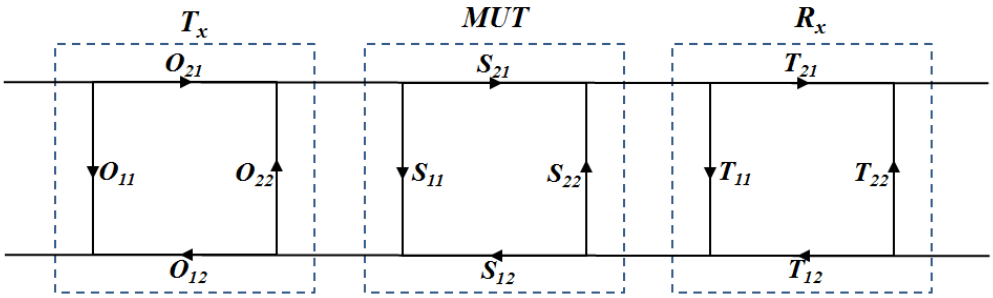

Figure 4.5: A model for the free-space transmission measurement consists of error coefficients and scattering parameters of MUT.

The GRL calibration is a time-domain calibration technique, which includes two fixtures of reflect and line (or empty standards, as shown in Figure 4.4. The signal flow graph of the GRL with the MUT is modeled in Figure 4.5. The S-parameters of the MUT can be obtained if the error coefficients, represented as an O matrix (O_{ii}) and a T matrix (T_{ii}), are calculated. There are eight unknowns; however, we can assume that $O_{12} = O_{21}$ and $T_{12} = T_{21}$ as the passive media are reciprocal, hence, the number of unknowns reduces to six. The experimental procedure is as follows:

1. Calibrate to the end of the PNA cables using the short-open-through-load (SOLT) method, or Ecal.

2. For the line fixture, measure the reflection coefficient at port 1, apply a time gate around the antenna and lens responses to collect O_{11}.

3. Repeat step 2 with the reflection coefficient at port 2 to collect T_{11}.

4. Subtract O_{11} from port 1's reflection coefficient to obtain Γ_{air1}, let $S_{11} = S_{22} = A_{11} = A_{22} = 0$ and $S_{12} = S_{21} = A_{12} = A_{21} = e^{-j\omega\sqrt{\mu\epsilon}d}$, where μ, ϵ are the permeability and permittivity of air, and d is thickness of the air gap, so as to obtain equation (4.1).

5. Repeat step 4 with the reflection coefficient at port 2 and T_{11} to get equation (4.2).

6. For the reflect standard, or metal-plate fixture, subtract O_{11} from port 1's reflection coefficient to obtain Γ_{metal1}, let $S_{11} = S_{22} = P_{11} = P_{22} = -1$ and $S_{12} = S_{21} = P_{12} = P_{21} = 0$, to obtain equation (4.3).

7. Repeat step 5 with the reflection coefficient at port 2 and T_{11} to acquire equation (4.4).

$$\Gamma_{air1} = \frac{A_{12}A_{21}O_{21}O_{12}T_{22}}{1 - O_{22}T_{22}}, \tag{4.1}$$

$$\Gamma_{air2} = \frac{A_{12}A_{21}T_{21}T_{12}O_{22}}{1 - O_{22}T_{22}}, \tag{4.2}$$

$$\Gamma_{metal1} = -\frac{O_{21}O_{12}}{1 + O_{22}}, \tag{4.3}$$

$$\Gamma_{metal2} = -\frac{T_{21}T_{12}}{1+_{22}}, \tag{4.4}$$

From four equations (4.1), (4.2), (4.3), (4.4), a quadratic equation with the unknown O_{22} is derived as follows

$$\begin{aligned} A_{12}A_{21}\Gamma_{metal2}(\Gamma_{metal1}A_{12}A_{21} - \Gamma_{air1})O_{22}^2 \\ + [A_{12}^2A_{21}^2\Gamma_{metal1}\Gamma_{metal2} + A_{12}A_{21}(\Gamma_{metal1}\Gamma_{air2} - \Gamma_{metal2}\Gamma_{air2})]O_{22} \\ + A_{12}A_{21}\Gamma_{air2}\Gamma_{metal1} = 0, \end{aligned} \tag{4.5}$$

Solving the equation, we obtain its root, O_{22}, by the condition that $|O_{22}|$ is not greater than unity. Substitute O_{22} into the four equations, and all the error coefficients are calculated. Once these O- and T-matrices are known, the MUT's scattering parameters can be derived from the signal-flow graph. First attempts on measuring the designed structure were made, and summarized in Appendix A.III.

Chapter 5

Conclusions

The realization of truly 3D metamaterials, which are able to interact with electromagnetic sources in free space, has drawn the attention of the physics and engineering communities for more than a decade. The main challenge for 3D metamaterials is the complexity of their physical implementation. Volumetric metamaterials are a solution for this problem because they are more easily constructed by stacking 2D metamaterials. Instead of interacting with an arbitrary source, however, they can couple to particularly polarized sources in free space.

The fabrication of volumetric metamaterials can be made simple by using fully-printed 2D metamaterial layers. In this thesis, a procedure to design a fully-printed volumetric NRI-TL is presented. An equivalent circuit model is developed, providing insight into the design and optimization of the structure in concert with full-wave simulations using HFSS. The metamaterial employs printed dual-arm spiral inductors and metal-insulator-metal capacitors as reactive loading elements; thus, it is suitable for standard lithography processes, rendering the manufacturing simple and inexpensive. In comparison with other printed structures, the proposed design operates at a lower frequency of $4.4GHz$ and achieves an electrical length of $\lambda_0/11$, where λ_0 is the

free space wavelength at the working frequency. Moreover, the structure is isotropic to 2D sources and possesses an effective permittivity and permeability close to negative unity at $4.4GHz$. However, the structure is lossy due to the printed loading inductors; this is inevitable for current fabrication technology. In future, along with the advance of technology, there may be printed inductors that have higher inductance values and quality factors; and they should be employed in the structure, so that they are less lossy. Thesis proposed an experimental scheme for measuring the designed structure including measurement setup, and tools for postprocessing the data. Although the preliminary results in Appendix A.III do not provide the expected responses of the structure, they help point out the potential source of errors, which will be useful for future study.

The proposed volumetric metamaterial may find applications in microwave hyperthermia and in the improvement of antenna performance. Moreover, the design procedure of the structure may be utilized for redesign the metamaterial in other frequency regimes, such as the terahertz regime. At terahertz frequencies, the structure requires smaller reactive loads, hence, the MIM-type capacitors can employ reduced parallel-plate length. For weaker loading inductance, the printed inductors may be implemented as a small conducting strip. Because the structure is multilayer, it will demand multiple depositions, rendering its fabrication complicated. However, the structure may find application as a 2D metamaterial for THz modulators or sensors, because the fabrication for a single layer is not complex.

There is no doubt that metamaterials has been a promising research area for the last decade. As the theory of metamaterials becomes more and more robust, it renders metamaterials useful in many applications not only in the microwave regime, but higher-frequency ranges, such as millimeter wave, terahertz, and even optics.

Bibliography

[1] N. Engheta and R. W. Ziolkowski, *Metamaterials: physics and engineering explorations.* Wiley. com, 2006.

[2] W. Rotman, "Plasma simulation by artificial dielectrics and parallel-plate media," *Antennas and Propagation, IRE Transactions on*, vol. 10, no. 1, pp. 82–95, 1962.

[3] J. B. Pendry, A. Holden, W. Stewart, and I. Youngs, "Extremely low frequency plasmons in metallic mesostructures," *Physical review letters*, vol. 76, no. 25, pp. 4773–4776, 1996.

[4] J. B. Pendry, A. Holden, D. Robbins, and W. Stewart, "Magnetism from conductors and enhanced nonlinear phenomena," *Microwave Theory and Techniques, IEEE Transactions on*, vol. 47, no. 11, pp. 2075–2084, 1999.

[5] R. Shelby, D. Smith, and S. Schultz, "Experimental verification of a negative index of refraction," *Science*, vol. 292, no. 5514, pp. 77–79, 2001.

[6] V. G. Veselago *et al.*, "The electrodynamics of substances with simultaneously negative values of ε and μ," *Physics-Uspekhi*, vol. 10, no. 4, pp. 509–514, 1968.

[7] G. V. Eleftheriades and K. G. Balmain, *Negative-refraction metamaterials: fundamental principles and applications.* Wiley-IEEE Press, 2005.

[8] J. B. Pendry, "Negative refraction makes a perfect lens," *Physical review letters*, vol. 85, no. 18, pp. 3966–3969, 2000.

[9] H. Lamb, "On group-velocity," *Proceedings of the London Mathematical Society*, vol. 2, no. 1, pp. 473–479, 1904.

[10] S. A. Schuster, *An introduction to the theory of optics*. E. Arnold, 1904.

[11] L. Mandelshtam, "Group velocity in a crystal lattice," *Zh. Eksp. Teor. Fiz*, vol. 15, no. 9, pp. 475–478, 1945.

[12] V. Pafomov, "On transition radiation and the Vavilov-Cherenkov radiation," *Zhur. Eksptl'. Teoret. Fiz.*, vol. 36, 1959.

[13] J. C. Bose, "On the rotation of plane of polarisation of electric waves by a twisted structure," *Proceedings of the Royal Society of London*, vol. 63, no. 389-400, pp. 146–152, 1898.

[14] I. V. Lindell, A. H. Sihvola, and J. Kurkijarvi, "Karl F. Lindman: The last Hertzian, and a harbinger of electromagnetic chirality," *Antennas and Propagation Magazine, IEEE*, vol. 34, no. 3, pp. 24–30, 1992.

[15] W. E. Kock, "Metal-lens antennas," *Proceedings of the IRE*, vol. 34, no. 11, pp. 828–836, 1946.

[16] ——, "Metallic delay lenses," *Bell Syst. Tech. J.*, vol. 27, pp. 58–82, 1948.

[17] S. Cohn, "Analysis of the Metal-Strip Delay Structure for Microwave Lenses," *Journal of Applied Physics*, vol. 20, no. 3, pp. 257–262, 1949.

[18] S. B. Cohn, "Experimental Verification of the Metal-Strip Delay-Lens Theory," *Journal of Applied Physics*, vol. 24, no. 7, pp. 839–841, 1953.

[19] J. Brown, "Artificial dielectrics," *Prog. Dielectr.*, vol. 2, pp. 195–225, 1960.

[20] R. E. Collin, *Field theory of guided waves*. IEEE press New York, 1991, vol. 2.

[21] D. H. Staelin, D. H. Staelin, A. W. Morgenthaler, and J. A. Kong, *Electromagnetic waves*. Pearson Education India, 1994.

[22] G. Kron, "Equivalent circuit of the field equations of Maxwell-I," *Proceedings of the IRE*, vol. 32, no. 5, pp. 289–299, 1944.

[23] G. V. Eleftheriades, A. K. Iyer, and P. C. Kremer, "Planar negative refractive index media using periodically LC loaded transmission lines," *Microwave Theory and Techniques, IEEE Transactions on*, vol. 50, no. 12, pp. 2702–2712, 2002.

[24] S. Ramo, J. R. Whinnery, and T. Van Duzer, *Fields and waves in communication electronics*. Wiley. com, 2007.

[25] A. Grbic and G. V. Eleftheriades, "Dispersion analysis of a microstrip-based negative refractive index periodic structure," *Microwave and Wireless Components Letters, IEEE*, vol. 13, no. 4, pp. 155–157, 2003.

[26] ——, "Periodic analysis of a 2-D negative refractive index transmission line structure," *Antennas and Propagation, IEEE Transactions on*, vol. 51, no. 10, pp. 2604–2611, 2003.

[27] F. Elek and G. V. Eleftheriades, "A two-dimensional uniplanar transmission-line metamaterial with a negative index of refraction," *New Journal of Physics*, vol. 7, no. 1, p. 163, 2005.

[28] A. K. Iyer and G. V. Eleftheriades, "Volumetric layered transmission-line metamaterial exhibiting a negative refractive index," *JOSA B*, vol. 23, no. 3, pp. 553–570, 2006.

[29] A. Grbic and G. V. Eleftheriades, "An isotropic three-dimensional negative-refractive-index transmission-line metamaterial," *Journal of applied physics*, vol. 98, no. 4, pp. 043 106–043 106, 2005.

[30] W. J. Hoefer, P. P. So, D. Thompson, and M. M. Tentzeris, "Topology and design of wideband 3D metamaterials made of periodically loaded transmission line arrays," in *Microwave Symposium Digest, 2005 IEEE MTT-S International*. IEEE, 2005, pp. 4–pp.

[31] P. Alitalo, S. Maslovski, and S. Tretyakov, "Experimental verification of the key properties of a three-dimensional isotropic transmission-line superlens," *Journal of applied physics*, vol. 99, no. 12, pp. 124 910–124 910, 2006.

[32] M. Zedler, C. Caloz, and P. Russer, "A 3-D isotropic left-handed metamaterial based on the rotated transmission-line matrix (TLM) scheme," *Microwave Theory and Techniques, IEEE Transactions on*, vol. 55, no. 12, pp. 2930–2941, 2007.

[33] A. K. Iyer and G. V. Eleftheriades, "A three-dimensional isotropic transmission-line metamaterial topology for free-space excitation," *Applied Physics Letters*, vol. 92, no. 26, pp. 261 106–261 106, 2008.

[34] S. M. Rudolph and A. Grbic, "A broadband three-dimensionally isotropic negative-refractive-index medium," *Antennas and Propagation, IEEE Transactions on*, vol. 60, no. 8, pp. 3661–3669, 2012.

[35] A. K. Iyer and G. V. Eleftheriades, "A Multilayer Negative-Refractive-Index Transmission-Line (NRI-TL) Metamaterial Free-Space Lens at X-Band," *Antennas and Propagation, IEEE Transactions on*, vol. 55, no. 10, pp. 2746–2753, 2007.

[36] ——, "Free-space imaging beyond the diffraction limit using a Veselago-Pendry transmission-line metamaterial superlens," *Antennas and Propagation, IEEE Transactions on*, vol. 57, no. 6, pp. 1720–1727, 2009.

[37] S. M. Rudolph and A. Grbic, "Volumetric negative-refractive-index medium exhibiting broadband negative permeability," *Journal of applied physics*, vol. 102, no. 1, pp. 013 904–013 904, 2007.

[38] M. Stickel, F. Elek, J. Zhu, and G. V. Eleftheriades, "Volumetric negative-refractive-index metamaterials based upon the shunt-node transmission-line configuration," *Journal of Applied Physics*, vol. 102, no. 9, pp. 094 903–094 903, 2007.

[39] S. M. Rudolph and A. Grbic, "Super-resolution focusing using volumetric, broadband NRI media," *Antennas and Propagation, IEEE Transactions on*, vol. 56, no. 9, pp. 2963–2969, 2008.

[40] S. M. Rudolph, C. Pfeiffer, and A. Grbic, "Design and free-space measurements of broadband, low-loss negative-permeability and negative-index media," *Antennas and Propagation, IEEE Transactions on*, vol. 59, no. 8, pp. 2989–2997, 2011.

[41] M. Selvanayagam and G. Eleftheriades, "Dual-Polarized Volumetric Transmission-Line Metamaterials," 2013.

[42] M. A. Antoniades and G. V. Eleftheriades, "A CPS leaky-wave antenna with reduced beam squinting using NRI-TL metamaterials," *Antennas and Propagation, IEEE Transactions on*, vol. 56, no. 3, pp. 708–721, 2008.

[43] ——, "A folded-monopole model for electrically small NRI-TL metamaterial antennas," *Antennas and Wireless Propagation Letters, IEEE*, vol. 7, pp. 425–428, 2008.

[44] A. Erentok and R. W. Ziolkowski, "Two-dimensional efficient metamaterial-inspired electrically-small antenna," *Microwave and optical technology letters*, vol. 49, no. 7, pp. 1669–1673, 2007.

[45] J. Zhu and G. Eleftheriades, "Dual-band metamaterial-inspired small monopole antenna for WiFi applications," *Electronics letters*, vol. 45, no. 22, pp. 1104–1106, 2009.

[46] G. Wang, J. Fang, and X. Dong, "Resolution of near-field microwave target detection and imaging by using flat LHM lens," *Antennas and Propagation, IEEE Transactions on*, vol. 55, no. 12, pp. 3534–3541, 2007.

[47] H. A. Atallah and E. K. Hamad, "Radiation pattern improvement of RDRA using LHM flat lens composed of CSRR," in *Antennas and Propagation (MECAP), 2010 IEEE Middle East Conference on*. IEEE, 2010, pp. 1–5.

[48] L. Brillouin, *Wave propagation in periodic structures: electric filters and crystal lattices*. Dover-Publications. com, 2003.

[49] P. Markoš and C. Soukoulis, "Transmission properties and effective electromagnetic parameters of double negative metamaterials," *Opt. Express*, vol. 11, no. 7, pp. 649–661, 2003.

[50] Rogers Corporation. (2013) RT/duroid 6006/6010LM High Frequency Laminates. [Online]. Available: http://www.rogerscorp.com/documents/612/acm/RT-duroid-6006-6010-laminate-data-sheet

[51] ——. (2011) RO3003 Series Circuit Materials. [Online]. Available: https://www.rogerscorp.com/documents/722/acm/RO3000-Laminate-Data-Sheet-RO3003-RO3006-RO3010.pdf

[52] Agilent Technologies. (2013) GRL calibration. [Online]. Available: http://www.home.agilent.com/agilent/home.jspx?cc=CA&lc=eng

[53] P. F. Goldsmith *et al.*, *Quasioptical systems*. Ediciones Díaz de Santos, 1998.

Appendices

A.I Periodic Structures

The Bravais lattice is an infinite array of discrete points, which can be used to represent a periodic structure. The Bravais lattice can be defined by translation operators of three-dimensional vectors, spanning the entire lattice. The translation operations formulated by a set of vectors $\overrightarrow{R}$ are described as

$$\overrightarrow{R} = n_1\overrightarrow{a_1} + n_2\overrightarrow{a_2} + n_3\overrightarrow{a_3}, \tag{5.1}$$

where a_i are non-zero vectors, and n_i are integers. This set is closed under the addition of vectors.

A plane wave propagating through the lattice has a form of $e^{j\overrightarrow{k}\cdot\overrightarrow{r}}$, where $\overrightarrow{k}$ is the wavevector of the plane wave, and vector $\overrightarrow{r}$ indicates a point of interest. Provided that the plane wave and the lattice have the same periodicity, the following equation is satisfied

$$e^{j\overrightarrow{k}\cdot(\overrightarrow{r}+\overrightarrow{R})} = e^{j\overrightarrow{k}\cdot\overrightarrow{r}}, \tag{5.2}$$

hence,

$$e^{j\overrightarrow{k}\cdot\overrightarrow{R}} = 1. \tag{5.3}$$

As a result, the reciprocal lattice is defined mathematically as a set of vectors $\overrightarrow{k}$, from now on termed $\overrightarrow{G}$, that satisfies the equation 5.3. The reciprocal lattice vector $\overrightarrow{G}$ is determined as

$$\overrightarrow{G} \cdot \overrightarrow{R} = 2\pi N, \tag{5.4}$$

where N is an integer, yielding,

$$\overrightarrow{G} = n_1' \overrightarrow{b_1} + n_2' \overrightarrow{b_2} + n_3' \overrightarrow{b_3}, \tag{5.5}$$

where n_i' are integers, and the basis vector b_i are

$$\overrightarrow{b_1} = 2\pi \frac{\overrightarrow{a_2} \times \overrightarrow{a_3}}{\overrightarrow{a_1} \cdot (\overrightarrow{a_2} \times \overrightarrow{a_3})}, \tag{5.6}$$

$$\overrightarrow{b_2} = 2\pi \frac{\overrightarrow{a_3} \times \overrightarrow{a_1}}{\overrightarrow{a_2} \cdot (\overrightarrow{a_3} \times \overrightarrow{a_1})}, \tag{5.7}$$

$$\overrightarrow{b_3} = 2\pi \frac{\overrightarrow{a_1} \times \overrightarrow{a_2}}{\overrightarrow{a_3} \cdot (\overrightarrow{a_1} \times \overrightarrow{a_2})}. \tag{5.8}$$

A primitive cell, also called Wigner-Seitz cell, is the smallest-volume cell that contains lattice points and other points in space that are closer to these lattice points than to any of adjacent lattice points. The Wigner-Seitz cell in the reciprocal lattice of a periodic structure is regarded as the Brillouin Zone. A simple cubic Brillouin zone with edge length d is depicted in Figure 5.1. The irreducible Brillouin zone is minimum part of the Brillouin zone, which is reduced by all of its symmetries such

as mirror symmetry, rotation symmetry, and inversion symmetry. The vertices of the irreducible Brillouin zone are determined as $\Gamma(0,0,0)$, $X(\pi,0,0)$, $M(\pi,\pi,0)$, and $R(\pi,\pi,\pi)$.

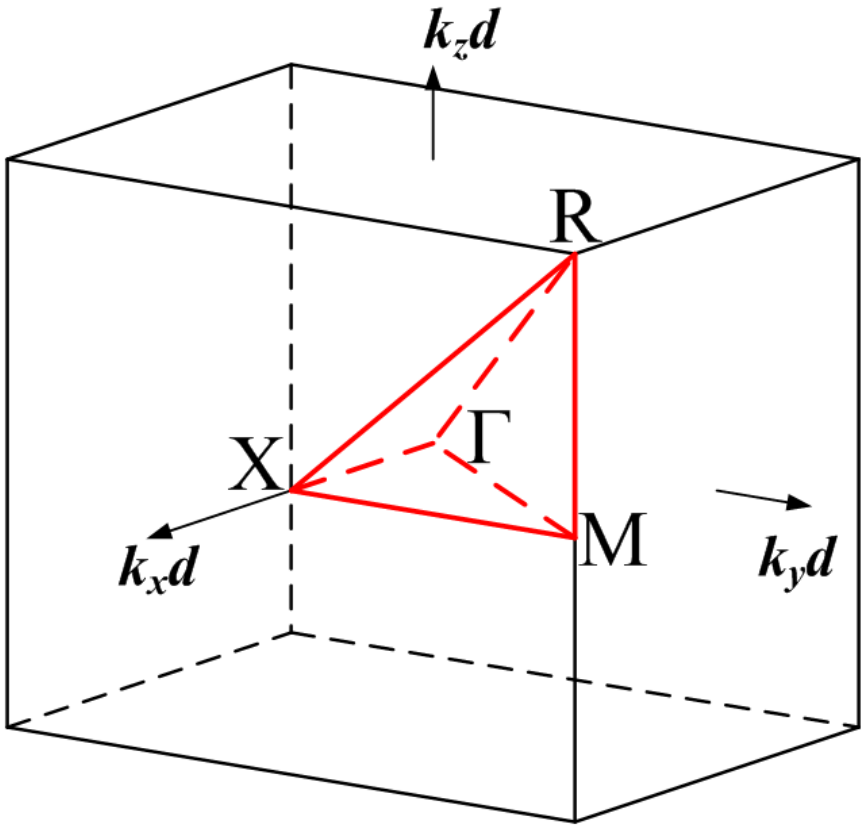

Figure 5.1: Brillouin zone and irreducible Brillouin zone (bounded by red lines) of a simple cubic lattice.

The cubic cell has an edge length of d, hence, the translation vector $\overrightarrow{R}$ of the lattice is defined as

$$\overrightarrow{R} = d \times (n_1(1,0,0) + n_2(0,1,0) + n_3(0,0,1)), \tag{5.9}$$

hence, the reciprocal lattice vector G is

$$\overrightarrow{G} = \frac{2\pi}{d} \times (n_1'(1,0,0) + n_2'(0,1,0) + n_3'(0,0,1)), \tag{5.10}$$

The propagation properties of all points in the irreducible Brillouin zone adequately represent those of the entire lattice. Let consider the dispersion of the structure in one direction, say from Γ to X. The dispersion of the fundamental harmonic is depicted by the blue lines in the first, second, and third Brillouin zones ($0 \rightarrow \pi, \pi \rightarrow 2\pi, 2\pi \rightarrow 3\pi$). In the first Brillouin zone, the dispersion of other harmonics is also displayed by red and black lines. As shown in Figure 5.2, the dispersion properties of the lattice can be captured in the first Brillouin zones, since the second mode in the second zone is flipped to the first zone. Similarly, the third mode is also flipped from the third zone to the second zone, and thereafter to the first zone. By applying the same procedure to higher order modes in other Brillouin zone, all the modes, i.e. the dispersion properties, of the lattice are presented in the first Brillouin zone.

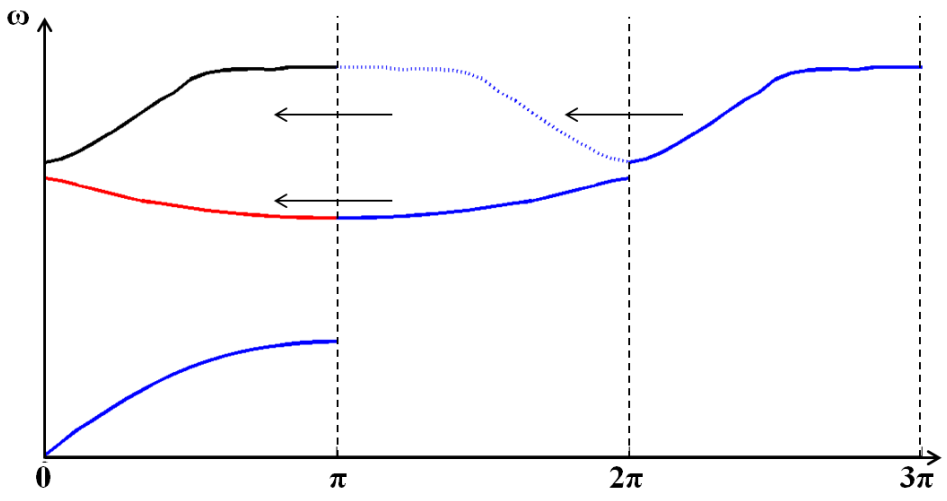

Figure 5.2: Dispersion properties of the lattice over a first three Brillouin zones.

The irreducible Brillouin zone contains all the dispersion properties of the first

Brillouin zone in all its points due to the symmetries. Therefore, investigation of these zones provides adequate information about the lattice. The one-dimensional lattice can be represented by a two-dimensional plot as the wavevector is scalar, and in a multi-dimensional lattice, its wavevector also has multiple dimensions, and hence, requires a multi-dimensional plot to visualize, which might be complicated. Fortunately, sampling the edges of the irreducible Brillouin zone suffices. An example of the graphical presentation of the dispersion relation is given as

$$\cos(\alpha) + \cos(\beta) + \cos(\delta) = 4 + \omega^2, \tag{5.11}$$

For sampling along the edge of Brillouin zone, the values of the variables α, β, and δ are as shown in Table 5.1:

TABLE 5.1: **Values of the variables along the edges of the irreducible Brillouin zone**

Edges	α	β	δ
$\Gamma \to X$	$0 \to \pi$	0	0
$X \to M$	π	$0 \to \pi$	0
$M \to \Gamma$	$\pi \to 0$	$\pi \to 0$	0
$\Gamma \to R$	$0 \to \pi$	$0 \to \pi$	$0 \to \pi$
$R \to M$	π	π	$\pi \to 0$

Figure 5.3 depicts the dispersion diagram of the simple cubic lattice that satisfies the dispersion relation in equation (5.11).

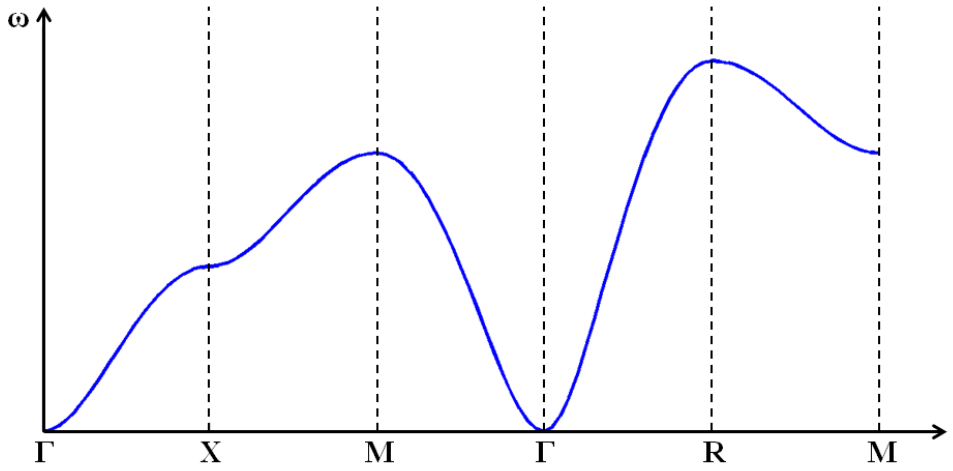

Figure 5.3: An example of dispersion diagram of the simple cubic lattice.

A.II Metallic Lenses

The lenses utilized in the experiment are metallic lenses proposed originally by Kock in Ref.[15]. These lenses have a positive refractive index smaller than unity. The guided waves that propagates through the lenses resemble TE modes in a parallel plate waveguide, for which the velocity is larger than the speed of light. The refractive index of the lenses is formulated as

$$n = \sqrt{1 - (\frac{\lambda}{2a})^2}, \tag{5.12}$$

where λ is the wavelength at operating frequency, and a is the gap between two plates. The gap between metal plates was filled with styrofoam with $3.81mm$ thickness, as shown in Figure 5.4, resulting in an overall effective index of refraction $n = 0.4487$.

The SGH antennas were positioned 31.3 cm away from the lens, which is the focal length at the antenna side of the lens and illuminated an area of effective diameter $w = 5\lambda = 34\ cm$. As shown in Figure 5.5, the metal lens was biconcave in order to

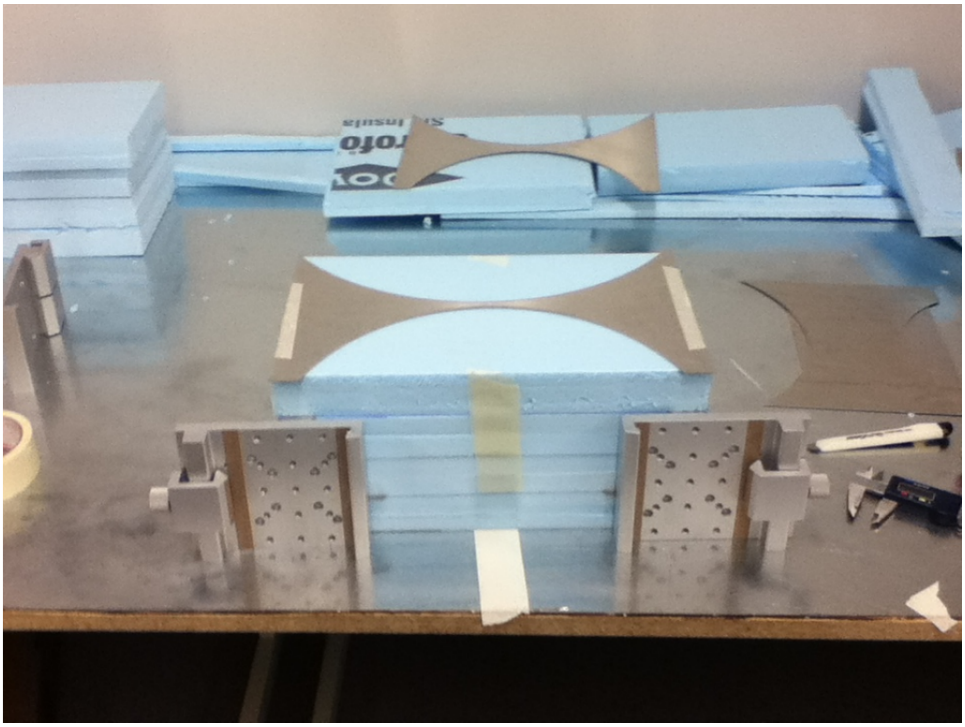

Figure 5.4: The fabrication of the metallic lens.

receive antenna field at one side, and to concentrate it at the other side. The MUT was placed at the focal point of the lenses, so that confined fields from the antenna propagated through the MUT as a plane wave with Gaussian beam profile with the waist radius of $\lambda/2$ (within a paraxial approximation). The distance between the lens and the MUT is the lens' focal length of 21.5 cm. Because the lenses have a thickness $d_2 = 20$ cm, the distances from the edges of the lenses to the SGH antennas and the MUT are $d_3 = 21.64$ cm and $d_1 = 10.9$ cm, respectively. The metal plates of the lens have an ellipsoidal profile with dimensions depicted in Figure 5.5. The detailed design procedure for the lenses can be found in Ref.[15, 53].

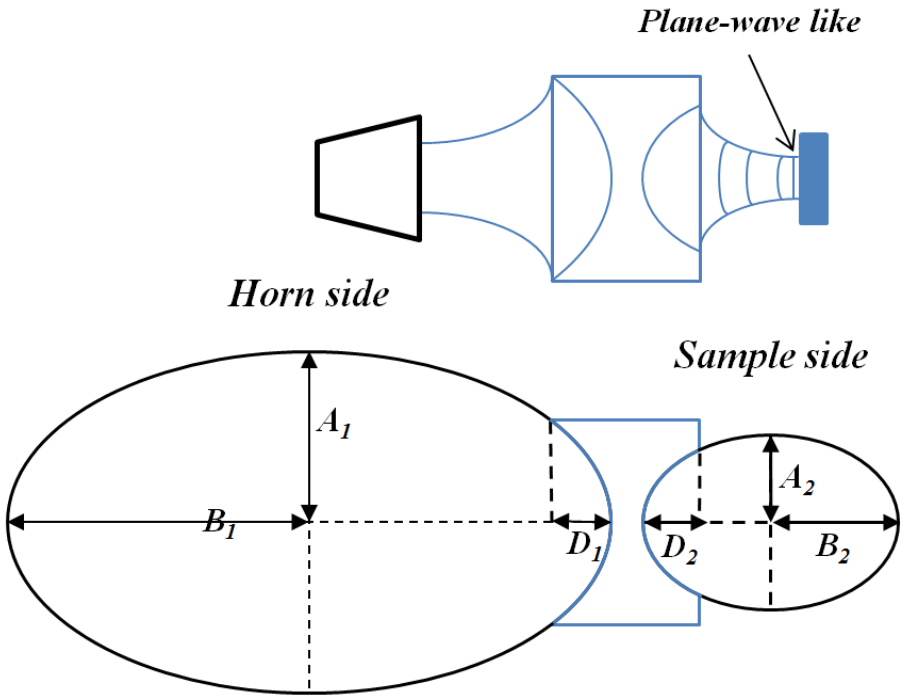

Figure 5.5: The dimensions of the bi-concave metal lens $A_1 = 18.92\ cm, B_1 = 21.16\ cm, D_1 = 9.56\ cm, A_2 = 14.45\ cm, B_2 = 16.16\ cm, D_2 = 10.6\ cm$.

A.III Preliminary Experimental Data

The first attempts on measurements of the MUT were conducted. The collected data for reflect, line fixtures and scattering parameters of the MUT are depicted in Figures 5.6 and 5.7.

For the data processing, an in-house Inverse Fast Fourier Transform (IFFT) code was produced to transform the responses from frequency domain into the time domain. Figure 5.8 depicts the response of reflection coefficient of the first SGH antenna in time domain. The peaks are identified as the reflection of EM wave by the first SGH antenna, and lenses. The gating position is selected by introducing a metal plate between the two lenses, and moving it toward the first lens, as shown in Figure 5.9. This helps find the position where the sample is placed (the red line). Because the

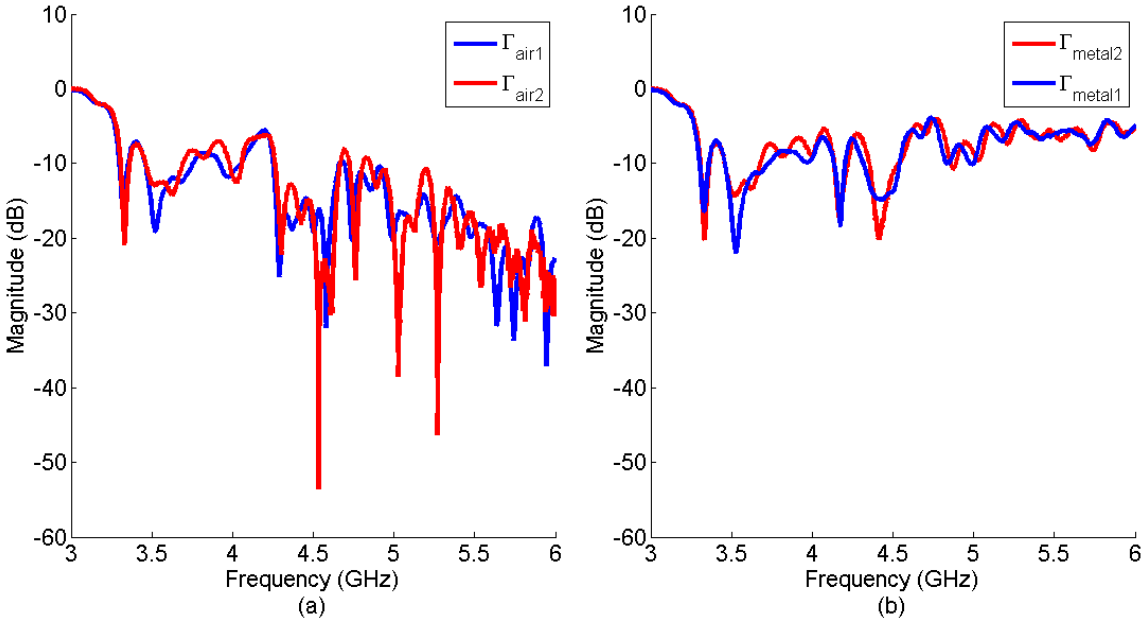

Figure 5.6: Reflection coefficients of the two SGH antennas in line fixture (a) and reflect fixture (b).

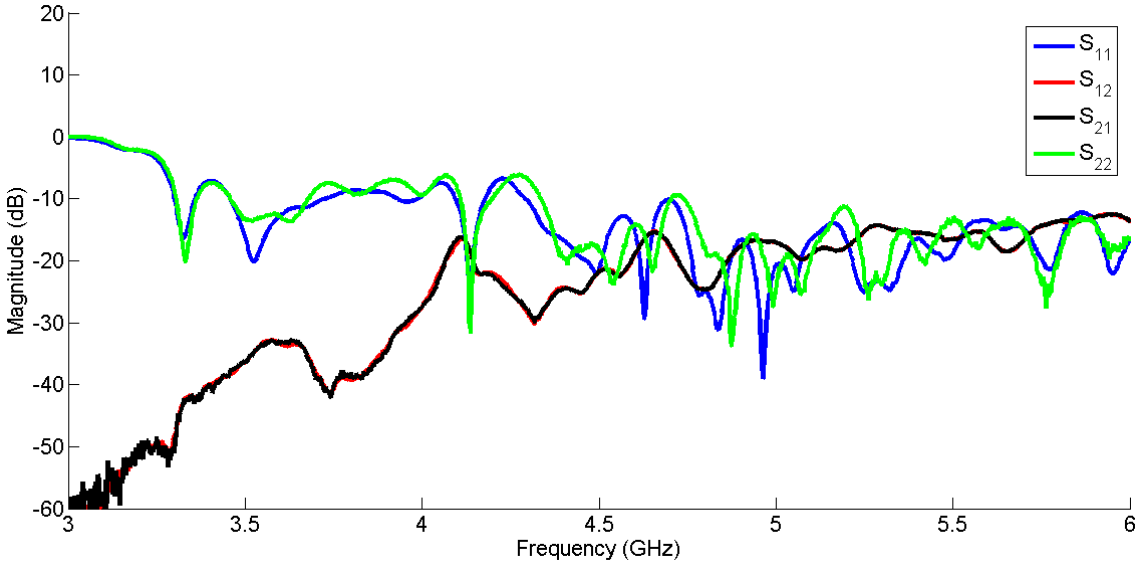

Figure 5.7: Measured scattering parameters of the MUT by the PNA.

gating function of the PNA is no longer available, the IFFT code can generate a window, which acts like "a low-pass filter" in time domain as time gate. The gated reflection coefficients of the first antenna in both time and frequency domains are depicted in Figure 5.10.

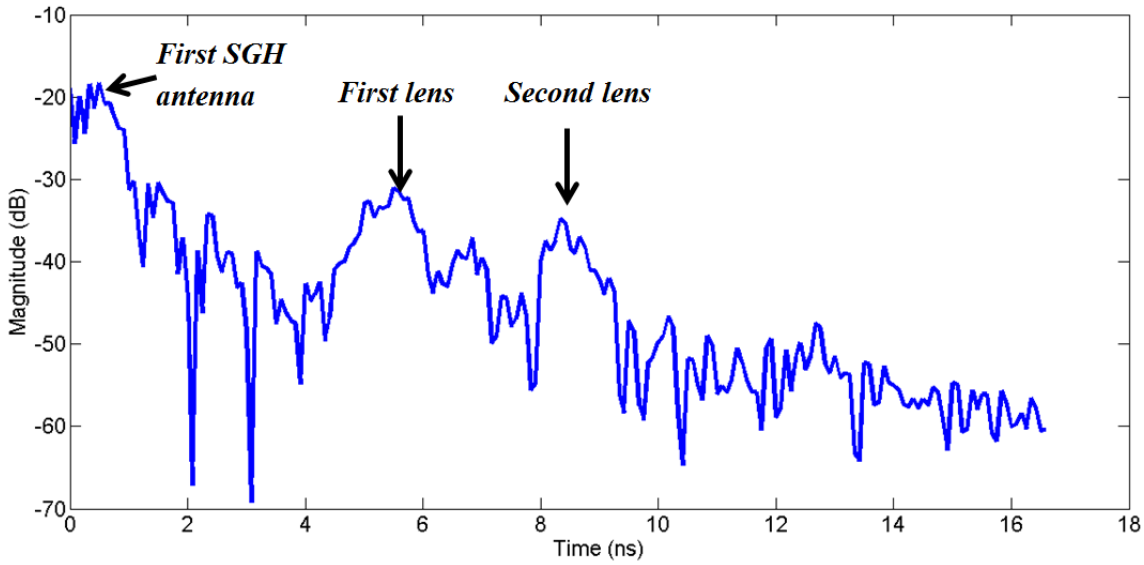

Figure 5.8: Transformed Γ_{air1} in time domain.

The extracted data for the MUT are displayed in Figure 5.11. The data show the right response at lower frequencies, which are below the cut-off frequency of the SGH antennas. However, they exhibit unreasonable behaviours at the frequency range of interest, where the metallic lenses operate. However, these lenses were examined independently to verify their performance, so that the possibility that they malfunction can be rule out. Moreover, the extracting procedure was tested on another set of data, which is collected at higher frequencies, and with conventional dielectric lenses. This suggests that the extraction procedure using metallic lenses needs further investigation. Additionally, the time-gating function of the IFFT code also needs better development, so that the time gate has a more practical responses.

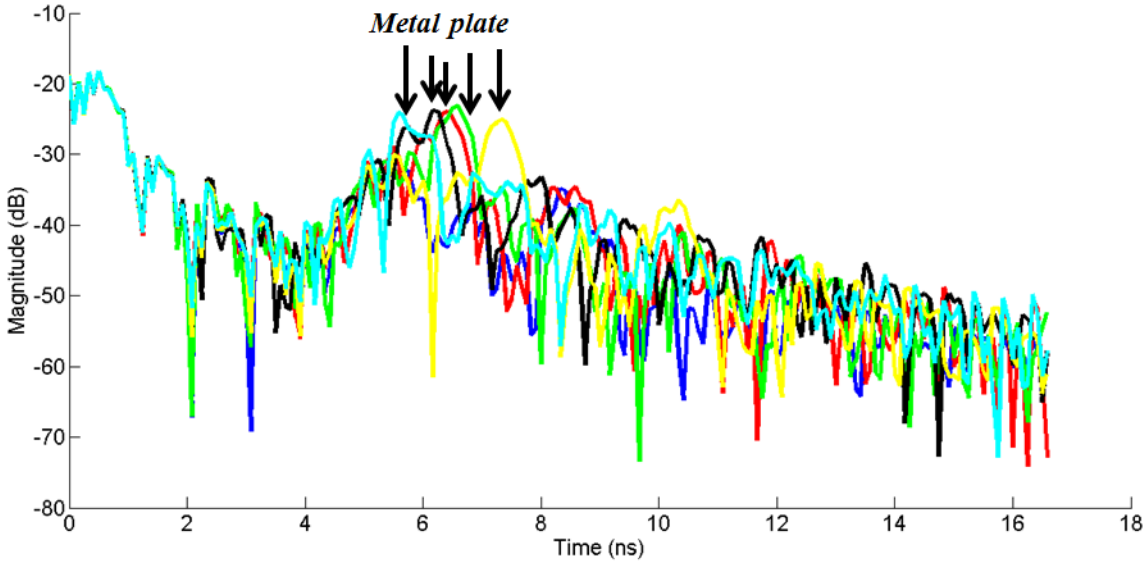

Figure 5.9: Transformed Γ_{air1} in time domain with the introduction of a metal plate.

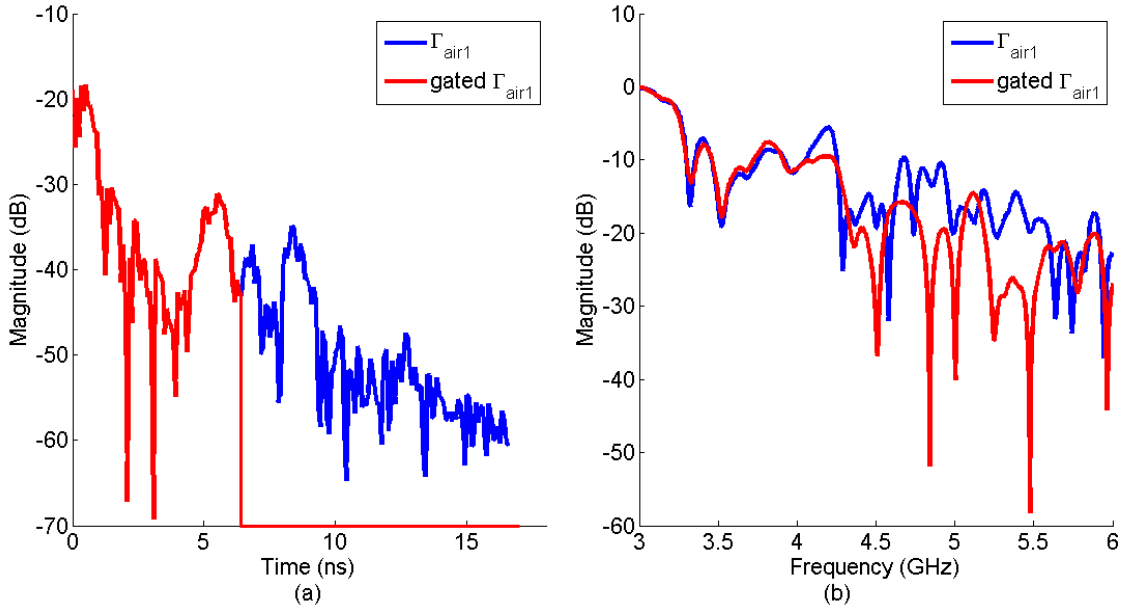

Figure 5.10: Gated Γ_{air1} in time domain (a) and frequency domain (b).

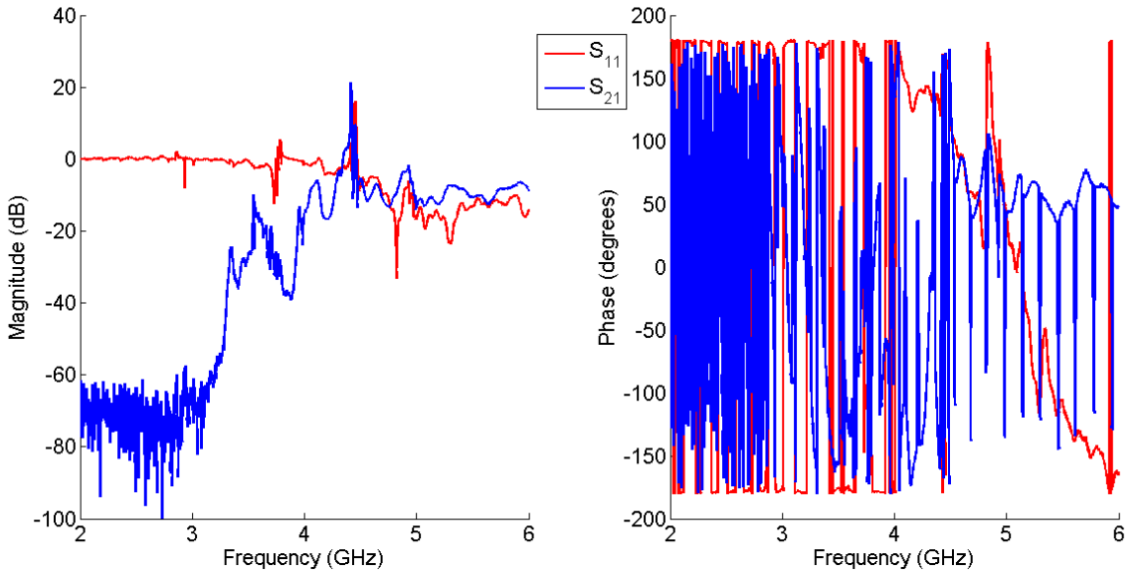

Figure 5.11: Extracted scattering parameters of the MUT.